

Astrophysical Journal, accepted

Models for Old, Metal-Poor Stars with Enhanced α -Element Abundances. III. Isochrones and Isochrone Population Functions

Peter A. Bergbusch

Dept. of Physics, University of Regina, Regina, Saskatchewan, S4S 0A2, Canada

Electronic mail: bergbush@phys.uregina.ca

and

Don A. VandenBerg

Dept. of Physics & Astronomy, University of Victoria, P.O. Box 3055, Victoria, B.C., V8W 3P6,
Canada

Electronic mail: davb@uvvm.uvic.ca

ABSTRACT

An isochrone population function (IPF) gives the relative distribution of stars along an isochrone. IPFs contain the information needed to calculate both luminosity functions and color functions, and they provide a straightforward way of generating synthetic stellar populations. An improved algorithm for interpolating isochrones and isochrone population functions, based on the scheme introduced by Bergbusch & VandenBerg (1992, ApJS, 81, 163), is described. Software has been developed to permit such interpolations for any age encompassed by an input grid of stellar evolutionary tracks. Our first application of this software is to the models presented in this series of papers for 17 [Fe/H] values between -2.31 and -0.3 , with three choices of $[\alpha/\text{Fe}]$ at each iron abundance (specifically, 0.0, 0.3, and 0.6). [These models do not treat gravitational settling or radiative acceleration processes, but otherwise they are based on up-to-date physics. Additional grids will be added to this data base as they are completed.] The computer programs (written in FORTRAN 77) and the grids of evolutionary tracks which are presently available for processing by these codes into isochrones and IPFs are freely available to interested users. In addition, we add to the evidence presented in previous papers in this series in support of the T_{eff} and color scales of our models. In particular, the temperatures derived by Gratton et al. (1996, A&A, 314, 191) for local Population II subdwarfs with accurate (*Hipparcos*) parallaxes are shown to be in excellent agreement with those predicted for them, when the Gratton et al. [Fe/H] scale is also assumed. Interestingly, the locus defined by local subdwarfs and subgiants on the $(M_V, \log T_{\text{eff}})$ plane and the morphologies of globular cluster C-M diagrams are well matched by the present models, despite the neglect of diffusion — which suggests that some other process(es) must be at play to limit the

expected effects of gravitational settling on predicted temperatures. The three field halo subgiants in our sample all appear to have ages $\gtrsim 15$ Gyr, which is favored for the Galaxy’s most metal-poor globular clusters (GCs) as well. (The settling of helium and heavy elements in the central regions of stars is expected to cause about a 10% reduction in these age estimates: this effect should persist even if some process, such as turbulence at the base of the convective envelope, counteracts diffusion in the surface layers.) Furthermore, our isochrones accurately reproduce the Da Costa & Armandroff (1990, AJ, 100, 162) red-giant branch fiducials for M 15, NGC 6752, NGC 1851, and 47 Tuc on the $[M_I, (V - I)_0]$ -diagram. However, our models fail to predict the observed luminosities of the red-giant bump by ≈ 0.25 mag: this could be an indication that there is some amount of inward overshooting of convective envelopes in red giants. For consistency reasons, the Zinn & West (1984, ApJS, 55, 45) metallicities for intermediate metal-poor GCs ($-1.8 \gtrsim [\text{Fe}/\text{H}] \gtrsim -1.1$) seem to be preferred over recent spectroscopic results (based on the brightest cluster giants), suggesting that there is an inconsistency between current subdwarf and GC $[\text{Fe}/\text{H}]$ scales.

Subject headings: globular clusters: general, stars: evolution, stars: interiors, stars: Population II

1. Introduction

Most metal-poor stars have relatively high abundances of the so-called “ α -elements” (O, Ne, Mg, Si, S, Ar, Ca, and Ti) — which is to say that the number abundance ratios O/Fe, Ne/Fe, etc., are higher than one finds in the Sun (see, e.g., the reviews by Wheeler, Sneden & Truran 1989, Kraft 1994, and McWilliam 1997). For instance, Carney (1996) concluded from his review of the available observational data that globular clusters (GCs) with $[\text{Fe}/\text{H}] \lesssim -0.6$ are overabundant in the α -elements by a factor of about two (i.e., $[\alpha/\text{Fe}] \approx +0.3$ in the standard logarithmic notation). Since then, some GCs have been discovered to have solar proportions of these elements (see Brown, Wallerstein, & Zucker 1997). Moreover, recent field star studies (e.g., Nissen & Schuster 1997) have revealed a significant number of halo stars with $[\alpha/\text{Fe}] \approx 0.0$, though the majority of such stars show the same level of enhancement as is typically found in GCs. Given that the abundances of the individual α -elements appear to scale with the overall α -element abundance,¹

¹It is our impression from the scientific literature that the mean $[\alpha/\text{Fe}]$ value generally represents the abundance ratios determined for the *individual* α -elements to within 0.1 dex. Oxygen may turn out to be an exception to this rule, but current estimates of the abundance of this element have large error bars associated with them because they depend sensitively on which spectral features are analyzed: much higher O/Fe ratios are found from the ultraviolet OH bands (Israelian, Garcia Lopez, & Rebolo 1998, Boesgaard et al. 1999) than from the $\lambda 630.0, \lambda 636.4$ nm [O I] lines (Fulbright & Kraft 1999). In this investigation we assume that all of the α -elements, including oxygen, vary

the chemical composition of a globular cluster or Population II star is often described in terms of the two quantities $[\text{Fe}/\text{H}]$ and $[\alpha/\text{Fe}]$.

It goes without saying that the models which are used to interpret stellar data should be computed for the run of chemical abundances that is actually observed — and given that there are star-to-star differences in the abundances of the α -elements at a fixed iron content, it is important to treat such variations explicitly. Accordingly, a new grid of stellar evolutionary tracks has been computed by VandenBerg et al. (2000; hereafter referred to as Paper I) for 17 $[\text{Fe}/\text{H}]$ values between -2.3 and -0.3 assuming, in each case, $[\alpha/\text{Fe}] = 0.0, 0.3$, and 0.6 . These calculations have also taken into account the most important non-ideal effects in the equation of state as well as recent improvements to opacity data and nuclear reaction rates (though gravitational settling and radiative acceleration processes are not treated). Moreover, as fully discussed in Paper I, the properties of local subdwarfs, the loci for GC red giants on the $(M_{\text{bol}}, \log T_{\text{eff}})$ -plane as inferred from infrared photometry, and the luminosities of RR Lyrae variables as deduced from Baade-Wesselink, statistical parallax, and trigonometric parallax studies are reproduced quite well by the models. Reference should be made to that study for a full description of how variations in $[\alpha/\text{Fe}]$ affect the tracks and zero-age horizontal-branches, both at a fixed $[\text{Fe}/\text{H}]$ and as a function of $[\text{Fe}/\text{H}]$.

In Paper II, VandenBerg (2000) examined the implications of the new model grids for the ages of GCs and of field halo stars. The main results of that study are (1) the most metal-deficient clusters *and* field subgiants have ages $\gtrsim 14$ Gyr, (2) ages decrease with increasing $[\text{Fe}/\text{H}]$ (by 2–3 Gyr between $[\text{Fe}/\text{H}] \sim -2.3$ and ~ -1.3) (3) the dispersion in age at a fixed metallicity appears to be small (especially at $[\text{Fe}/\text{H}] \lesssim -1.3$), and (4) there is no more than a weak variation of age with Galactocentric distance, if that. However, the photometric data for many of the clusters are still not as good as they need to be, relative age estimates based on the horizontal method, as described by VandenBerg, Bolte, & Stetson (1990), sometimes seem to be inconsistent with those derived from the $\Delta V_{\text{TO}}^{\text{HB}}$ technique (suggesting that something besides, or in addition to, age is varying), and the uncertainties associated with most reddening, metallicity, and distance determinations remain large. Consequently, the conclusions that were reached must still be considered tentative even though they seem well-supported by the observations *as they presently exist*. (Many age-related issues, such as how best to intercompare synthetic and observed C-M diagrams for the determination of both absolute and relative ages, are discussed in Paper II.)

The primary purpose of the present investigation is to make the α -element enhanced isochrones and what we have called “isochrone population functions” (IPFs) readily available to the astronomical community. An IPF is derived from the slope of the predicted mass–*distance* relation in M_{\odot}/mag , where the distance along an isochrone, on any color–magnitude plane for

together. The possibility that $[\text{O}/\text{Fe}] \sim 1$ in extremely metal-deficient stars, and the consequences of such high oxygen abundances for synthetic C-M diagrams and for turnoff luminosity versus age relations, is considered by VandenBerg & Bell (2001).

which good color– T_{eff} relations are available, is defined with respect to some arbitrary, well-defined point. In conjunction with an assumed mass spectrum, IPFs thus provide the means to generate synthetic stellar populations in a very straightforward way or to calculate luminosity functions (LFs) or color functions (CFs). The value and importance of LFs have long been appreciated (see, e.g., Renzini & Fusi Pecci 1988), but it is only recently that Bergbusch & VandenBerg (1997) have pointed out that the distribution in color of stars along the subgiant branch has the potential to provide an age constraint that is not only completely distance-independent, but is also nearly metallicity-independent. To obtain meaningful results from observed CFs, superb photometry and very large subgiant samples are needed, but it should be possible to meet these requirements in the case of the nearest and most massive of the Galaxy’s GCs. Certainly, all aspects of observed C-M diagrams should be fully investigated in order to achieve the best possible understanding of stellar systems.

In the following section, an improved algorithm for interpolating in evolutionary sequences for isochrones and IPFs is described: this is based in large part on the scheme introduced by Bergbusch & VandenBerg (1992; hereafter BV92). Section 3 outlines how to execute the software that has been developed to obtain isochrones, IPFs, LFs, and CFs, and provides a fairly detailed description of the output of these codes. In §4, some additional discussion beyond that contained in Papers I and II is presented on how well the present computations appear to satisfy observational constraints. Brief concluding remarks are given in §5.

2. The Interpolation Algorithm

The mathematical formalism for the derivation of accurate IPFs parallels that for the derivation of luminosity functions presented in BV92, except that the distance along an isochrone is used as the observable coordinate instead of luminosity. In the $\log L$ – $\log T_{\text{eff}}$ plane, the distance along an isochrone is defined by

$$d\mathcal{D} = \left[c_1 (d \log L)^2 + c_2 (d \log T_{\text{eff}})^2 \right]^{1/2}, \quad (1)$$

where c_1 and c_2 are chosen to stretch the SGB region and to obtain a convenient range of distances. (We have chosen $c_1 = 1.25$ and $c_2 = 10.0$, and we arbitrarily define $\mathcal{D} = 0$ at the lowest mass point on the isochrone.) The slope of the mass–distance relation is then obtained from

$$\frac{d\mathcal{D}}{d\mathcal{M}} = \left[c_1 \left(\frac{\partial \log L}{\partial \mathcal{M}} \right)^2 + c_2 \left(\frac{\partial \log T_{\text{eff}}}{\partial \mathcal{M}} \right)^2 \right]^{1/2}. \quad (2)$$

Consequently, equation (6) from BV92 is recast as

$$\phi(\mathcal{D}) = N(\mathcal{M}) \left(\frac{d\mathcal{D}}{d\mathcal{M}} \Big|_t \right)^{-1}, \quad (3)$$

where $N(\mathcal{M})$ is the number of stars with mass \mathcal{M} , and $\phi(\mathcal{D})$ is the differential isochrone population function. (Note that the second of these two equations becomes the familiar definition of a differential luminosity function if \mathcal{D} is replaced by L — see BV92.) The evaluation of the partial derivatives in equation (2) is performed as described in BV92.

In the observer’s plane, the distance is calculated with respect to a well-defined, but arbitrary, point on the isochrone. For this paper, a point on the subgiant branch (SGB) 0.05 mag redward of the main-sequence turnoff (regardless of color index), has been adopted as the distance zero-point with the idea that it should be relatively easy to identify in observed CMDs. A convenient definition of distance is

$$dD = \left[dM_i^2 + 16 dC_{ik}^2 \right]^{1/2}, \quad (4)$$

where M_i is the absolute magnitude in the i^{th} passband and C_{ik} is the color index for passbands i and k . However, the transformation of equation (3) from the theoretical plane to the observer’s plane involves the derivatives of both the color transformations and the bolometric corrections. Rather than attempt to evaluate these numerically, it is easier to construct a \mathcal{D} – D calibration which can be used to translate bin limits from the observer’s plane to the theoretical plane, and then to perform integrations across bins on the theoretical plane.

2.1. Equivalent Evolutionary Phases

Isochrones, IPFs, LFs, and CFs are interpolated from grids of evolutionary tracks for stars of the same initial chemical composition but different masses. Consequently, the most fundamental interpolation is the one in which the mass is derived from the age–mass relation for a given evolutionary phase. The obvious advantage of an interpolation scheme in which mass is a monotonic function of age is that the mass is uniquely determined once the age and evolutionary phase are specified. The corresponding luminosities, effective temperatures, and their temporal derivatives then can be interpolated with respect to mass.

The basic approach to setting up the interpolation scheme remains as it was described in BV92, with up to seven primary “equivalent evolutionary phase” (EEP) points (see, in particular, their Fig. 2) located on each track between the zero-age main sequence and the tip of the RGB. The definitions of two of these points have been revised slightly. The first primary EEP is now taken to be the point at which the central hydrogen content falls to $X_i - 0.0022$, where X_i is the adopted H abundance in the initial fully convective model on the Hayashi line. This corresponds quite well with the zero-age main-sequence location of the model on the H–R diagram.

The more noteworthy change resulted from the discovery that the age–mass relation defined by the second primary EEPs can be non-monotonic just where the blue hook begins to manifest itself (at $\approx 1.15\mathcal{M}_\odot$), if the amount of convective overshoot is assumed to increase with increasing mass. (Depending on whether the star has a radiative or convective core during the main-sequence phase, the second primary EEP corresponds to either the turnoff point or the minimum T_{eff}

that is reached just prior to the blue hook, respectively.) It is however, relatively easy to avoid this difficulty. As shown in Figure 1, the competition between the p - p chain and the CNO cycle produces a small dip in the derivative $d \log T_{\text{eff}} / d \log t$ for the lower mass tracks that develops into the blue hook at higher mass. When this feature appears *after* the turnoff point, it is used to define the second primary EEP.²

Over the range 0.5 – $1.8 M_{\odot}$ in stellar mass and for metallicities $-2.31 \leq [\text{Fe}/\text{H}] \leq +0.12$ that we have investigated, the age–mass relations for the primary EEPs remain monotonic.³ Thus, it is possible to maintain the monotonic behaviour in the secondary EEP relations that are obtained by dividing each evolutionary phase interval, bracketed by a pair of primary EEPs, into an equal number of regularly placed sub-intervals. For the evolutionary tracks of low-mass stars which achieve ages of 30 Gyr before reaching the turnoff point, the placement of the last secondary EEP is determined by matching it with the secondary EEP having the same central hydrogen content on the track of the next higher mass.

2.2. The Akima Spline

In BV92, linear interpolation was found to be acceptable for all of the EEP relations, except for the evaluation of derivatives along the direction of interpolation. In the absence of a better solution at the time, these derivatives were evaluated from a cubic polynomial fitted through the EEP points — in other words, the derivatives were obtained from smoothed versions of the EEP relations. However, for this paper, the interpolations and evaluations of derivatives were performed with the Akima spline (Akima, 1970), for complete internal consistency. Among the various spline routines tested, the Akima spline was found to be the best for tracing the subtle morphology of the EEP relations, as it is particularly good at avoiding the typical spline overshooting that occurs when the behaviour of the spline points is non-polynomial. In addition, as one may infer from Fig. 6 of BV92, linear interpolation tends to produce the onset of the convective hook in the isochrones at ages slightly greater than those predicted by the evolutionary sequences. Akima spline interpolation reduces this discrepancy over the entire range of metallicities that we have investigated.

The differences between isochrones derived via Akima spline interpolation and those derived using linear interpolation can be readily appreciated by comparing the EEP relations that give the turnoff effective temperatures and luminosities as a function of mass. The T_{eff} EEP relations,

²Minor oscillations in the temperature derivative sometimes occur (e.g., those preceding the turnoff point in the $0.9 M_{\odot}$ track in Fig. 1). Perturbations to the model arising from the procedures used to optimize the mesh point distribution or to calculate the atmospheric boundary conditions are the most likely causes of this behavior. However, the amplitude of such variations is clearly very small and of little consequence for computed IPFs.

³Extensions of the present calculations to higher mass and $[\text{Fe}/\text{H}]$ will be the subject of a forthcoming paper by D.A. VandenBerg, P.A. Bergbusch, and P.D. Dowler (in preparation).

plotted in upper panel of Figure 2, reveal small, but detectable, differences between linear interpolation and Akima spline interpolation at the turnoff, even for low mass stars. Moreover, the largest differences always occur when there is an abrupt change in the behaviour of the EEP relation. For example, in the $[\text{Fe}/\text{H}] = -2.31$, $[\alpha/\text{Fe}] = 0.0$ grid, isochrones with ages 8 and 12 Gyr, interpolated by either method, are virtually identical at the turnoff because they have turnoff masses near 0.9 and 0.8 solar masses, respectively. However, the turnoff masses for ages 10, 14, and 16 Gyr, lie near $0.85\mathcal{M}_\odot$, $0.76\mathcal{M}_\odot$, and $0.74\mathcal{M}_\odot$, respectively; i.e., approximately midway between the computed tracks. The T_{eff} EEP relations shows a distinct change in slope at $0.8\mathcal{M}_\odot$, around which the spline deviates noticeably from the linear relations. As can be seen from the lower panel of Fig. 2, the difference in $\log T_{\text{eff}}$ for a mass of $0.76\mathcal{M}_\odot$ is ≈ 0.001 . This means that the temperature predicted by the Akima spline interpolation, for the turnoff of a 14 Gyr isochrone, is ≈ 15 K cooler than that derived by linear interpolation.

Similar observations can be made about the luminosity EEP relations, plotted in the upper panel of Figure 3. The differences in $\log L/L_\odot$ between the two interpolation methods, plotted in the lower panel, reveal that turnoff luminosities are consistent to within 0.02 mag in M_{bol} over the entire range of masses plotted, and to within 0.008 mag over the range of turnoff masses relevant to globular cluster studies.

It should be emphasized that the points plotted in the EEP relations of Figs. 2 and 3 are taken *directly* from the model tracks. In most instances, they were identified automatically by software designed to recognize the primary EEPs. Thus, they directly reflect the behaviour of the models at the masses specified. One problem that is exposed by the spline approach occurs as a result of the fact that there are usually more tracks with zero-age main sequence EEPs than turnoff EEPs, and more with turnoff EEPs than with EEPs on the subgiant branch (because lower mass tracks are not extended past an age of 30 Gyr). Consequently, the nature of the spline fit to the EEPs changes abruptly when the number of points used to construct the fit changes. This sometimes manifests itself as a small discontinuity on an isochrone generated via the Akima spline, that would not be evident on one generated by linear interpolation. (We emphasize that such discontinuities are virtually undetectable; we have ensured this by extending low mass tracks to the base of the RGB in the grids where discontinuities appeared on isochrones near the turnoff.)

While the Akima spline provides an accurate means of interpolating the points along an isochrone, its chief advantage over linear interpolation is that derivatives can be evaluated directly at each point. A comparison between differential IPFs on the theorist’s plane, derived from Akima spline interpolation via the approach defined by equations (2) and (3), and IPFs calculated directly from the tabulated masses and distances obtained via linear interpolation, is shown in Figure 4. The discontinuities evident on the main sequence portion of the linearly interpolated IPFs occur wherever an isochrone crosses one of the evolutionary tracks. They are caused by the abrupt changes in the slopes of the interpolation relations at these points. Such discontinuities would also be evident in linearly interpolated LFs and CFs; they did not appear in the LFs presented in BV92 because the slopes of the EEP relations were derived from cubic polynomial fits to the EEP

points.

2.3. Stability of the Models

First we describe the general morphology of the IPFs with respect to the expected evolutionary behavior, using the examples plotted in Figure 5. The transition from the main sequence to the RGB occurs near $D(I, B-I) = 0$ for both the metal-rich and the metal-poor cases, because the distance, as we have defined it, is calculated with reference to a point on the subgiant branch 0.05 mag redward of the turnoff. The relatively broad local maximum immediately following the transition, at $D(I, B-I) \approx -2$, corresponds to the inflection point in the temperature evolution at the base of the RGB. The evolutionary pause on the RGB is located at a distance near -5 to -6 in both cases. The extension of the upper RGB to distances beyond -20 in the $[\text{Fe}/\text{H}] = +0.12$ grid occurs because giant branch evolution in color is stronger than in more metal-poor stars, and color evolution is weighted more strongly than luminosity evolution in the calculation of distance along an isochrone.

In the theorist’s plane, the derivatives of luminosity and temperature with respect to time along evolutionary sequences tend to have some numerical noise on the lower RGB, more obviously in the metal-rich grids. The very fine wiggles seen on the lower RGB portion of the interpolated metal-rich IPF plotted in the upper panel of Fig. 5 are a manifestation of this.

All of the other structures not predicted by canonical theory arise from the adopted color– T_{eff} relations and the bolometric corrections. This is particularly evident at the faint end of the models in the upper panel of Fig. 5, where the plateau-like structure near $D = +10$ in the IPF has no counterpart at the faint end of the theorist’s IPFs plotted in Fig. 4. Similar irregularities can be seen on the upper RGB, such as the one that is weakly evident near $D = -10$ in the upper panel. It turns out that this anomaly is also found near $B-I = 3.4$ in the corresponding CF (not shown), and that it occurs over the same range in $(B-I)$ as the plateau-like structure on the main sequence. Moreover, artifacts of the bolometric corrections, evident near the bright and faint ends of the corresponding LF (not shown), are also found to occur over the same range in $(B-I)$.

One conclusion that can be drawn from Fig. 5 is that neither the color– T_{eff} relations nor the bolometric corrections are solely responsible for a number of the features on the computed IPFs. Most of them are probably not real; indeed, it is our impression that the transformations to the observed plane are not as consistently determined for the metal-rich grid as for the metal-poor grid. For instance, only very minor artifacts appear on the IPFs for the latter case. The small glitch near $D = -5$ on the IPF can be traced to a corresponding glitch near $B-I = 1.6$ on the CFs, etc. Comparisons with observations are needed for definitive conclusions: at this point, we can only say that, for the metal-rich grids in particular, the discontinuous behavior on both the main-sequence and on the RGB portions of the CFs between $3.2 \lesssim B-I \lesssim 3.8$, and the corresponding wiggles at the bright and faint ends of the LFs originate in the same $\log T_{\text{eff}}$ region of the transformation

tables in which the color indices and bolometric corrections are interpolated.⁴

3. Tabulations of the Models

For this paper, the grids of evolutionary tracks described in Paper I have already been processed with software that automatically locates the primary EEPs.⁵ In this section, we describe how to use the software and we give examples of the file formats currently available.

Each grid of models is contained in an EEP file (denoted by the file extension .eep) with the format illustrated in Table 1. The first seven lines have the same format in all of the subsequent files produced from the EEP file. The first line specifies that this particular file contains seven tracks; lines 2 through 6 list the adopted chemical abundances and line 7 gives the assumed mixing length parameter. For each track, there is a header line listing the mass, the number of models in the track (**Npts**), the last model generated via the Lagrangian code (**Match**), the shifts in age and in $\log T_{\text{eff}}$ applied to the subsequent giant branch models computed via the Eggleton (1971) method⁶, the age of the first model on the track, and the model numbers of the primary EEPs. In the example illustrated, the primary EEPs for the $1.1M_{\odot}$ track are located at models 1, 36, 134, 198, 278, and 434 — this track does not have a convective hook and thus the three spaces following the turnoff point (36) are blank. Within each track, the entries are the model number, the luminosity, the effective temperature, the age, the central hydrogen content, the derivative of luminosity with respect to time, and the derivative of the effective temperature with respect to time.

Iochrones on the $\log L$ – $\log T_{\text{eff}}$ plane are generated with the program MKISO, which interactively prompts the user for the input EEP file and a series of isochrone ages. Table 2 illustrates the format of the isochrone files (denoted by the extension .iso) generated. The first line indicates that the file contains 6 isochrones. The header line for each isochrone lists its age and the number of points generated. The individual lines for each isochrone list the luminosity, the effective temperature, the mass, the distance along the isochrone, and two values of the derivative

⁴We suspect that some improvement in the methods used to interpolate in these tables could reduce the noise arising from this source. It is our intention to check into this possibility when the extension of the present grids to $[\text{Fe}/\text{H}] > -0.3$ is prepared for publication.

⁵The software (written in FORTRAN 77) to produce isochrones, IPFs, LFs, and CFs, as well as the input .eep files for the evolutionary tracks presented in this series of papers are available on request: contact P. Bergbusch via email at bergbus@phys.uregina.ca.

⁶As described by VandenBerg (1992), the University of Victoria code employs the usual Henyey method to solve the stellar structure equations, with mass as the independent variable, when dealing with evolutionary phases prior to the lower RGB. Thereafter, the non-Lagrangian technique developed by Eggleton (1971) is used (for efficiency reasons) to extend the tracks to the tip of the giant branch.

of the mass with respect to distance along the isochrone. The first of these values is computed via equation (2); the second is computed directly via five point differentiation along the isochrone.

Isochrones, IPFs, LFs, and CFs are generated with the program MKIPF, which prompts the user for the input isochrone file, the passband (B , V , R , or I) for the magnitudes, the color index ($B-V$, $B-R$, $B-I$, $V-R$, or $V-I$), and three values for the exponent, x , in the power law mass spectrum given by $N(\mathcal{M}) \propto \mathcal{M}^{(1+x)}$. The user then specifies the type of output desired and is asked to specify the bin size. For example, if the option to produce an IPF file (with the extension .ipf) is chosen, the bin size is specified in terms of the distance along the isochrone, in whatever passband and color index were selected; if the LF option (with the extension .lfn) is chosen, the bin size is specified in terms of the passband selected; if the CF option (with the extension .cfn) is chosen, the bin size is specified in terms of the color index selected.

The format of an IPF file is shown in Table 3. In this example, the magnitude passband and the color index selected were I and $V-I$, respectively. The three values supplied for the mass-spectrum exponent were -0.5 , $+0.5$, and $+1.5$. For each age specified in the input isochrone file, the isochrones and IPFs are tabulated at equal distance intervals. The entries on a line are the magnitude, the color index, the mass, the bolometric magnitude, $\log T_{\text{eff}}$, $\log g$, the distance along the isochrone (the bin size is specified with respect to this distance), and three pairs of differential and cumulative (logarithmic) IPFs, one pair for each value of x specified. The last line for each age specified gives the parameters for a model at the RGB tip.

The format of an LF file is shown in Table 4. In this example, both the differential and cumulative distributions are tabulated at the centers of 0.2 mag bins, except for the bin at the RGB tip. The format of a CF file is almost the same. However, since stars in the post-turnoff stages of evolution have the same colors as those along the main sequence, the distributions have been separated at the color of the turnoff. For the example CF file shown in Table 5, there are 53 (N_{ms}) bins associated with the main sequence in the 8 Gyr model; the post-turnoff portion begins at bin 54.

4. Additional Tests of the Models

In order to make reliable stellar populations models, the predicted luminosity, T_{eff} , and color scales of the underlying evolutionary tracks and isochrones must be as accurate as possible. In this section, we describe some further tests of the theoretical calculations, beyond those presented in Papers I and II, which show that they seem to satisfy most observational constraints rather well.

4.1. The Subdwarf T_{eff} Scale

As discussed in Paper I, the value of the mixing-length parameter, α_{MLT} , that has been assumed in these calculations, was set by the requirement that a Standard Solar Model reproduce the observed temperature of the Sun. (To be consistent with the models presented in this series of papers, the reference solar model did not take diffusive processes into account.) In support of the resultant T_{eff} scale, it was shown that the location on the $(M_V, \log T_{\text{eff}})$ –plane of the well-observed subdwarf HD 103095 (perhaps better known by the name Groombridge 1830) is matched quite well by models for the appropriate chemical abundances if its temperature is $\gtrsim 5100$ K. Although there is considerable support for this estimate (e.g., King 1993; Gratton, Carretta, & Castelli 1996), many would argue that something closer to 5000 K is more realistic (see, e.g., Alonso, Arribas, & Martínez-Roger 1996; Balachandran & Carney 1996). Indeed, the effective temperatures of most stars, including the best-studied Population II subdwarfs, appear to be uncertain at the level of about 100 K, which clearly limits the ability of such data to provide stringent constraints on predicted T_{eff} scales.

However, it is worthwhile to explore this issue further — for the following reason. Paper I concluded that the present models provide a good fit to the local subdwarfs on the $[M_V, (B-V)_0]$ –diagram, *if* metallicities close to those adopted by Gratton et al. (1997) are assumed for them. But whether or not comparable agreement is found on the $[M_V, \log T_{\text{eff}}]$ –plane, if the *temperatures* derived by Gratton et al. are assumed, was not investigated. In fact, it turns out that there is quite good consistency between these two plots. To illustrate this, we have constructed “mono-metallicity” subdwarf sequences consisting of those subdwarfs that have the smallest uncertainties in their parallaxes, along with a few subgiants to permit an evaluation of the ages of stars that have evolved past the main-sequence turnoff. That is, we have used our isochrones (only in a differential sense) to correct the inferred T_{eff} and intrinsic color of each field halo star, at its observed M_V , to the temperature and color it would have if it had $[\text{Fe}/\text{H}] = -2.31$. (We chose the lowest metallicity in our grid as the reference $[\text{Fe}/\text{H}]$ value because the few subgiants that we have considered are very metal-deficient and it is desirable that the T_{eff} /color adjustments which are applied to them be as small as possible to avoid introducing significant errors into the determination of their ages.)

The result of this exercise on the $[M_V, \log T_{\text{eff}}]$ –plane is shown in Figure 6. The M_V , $\sigma(M_V)$, and $[\text{Fe}/\text{H}]$ values that have been adopted are from the updated list of parameters given by Carretta et al. (2000),⁷ while the sources of the temperature data are Gratton et al. (1996) and,

⁷Their entry for the parallax of the essentially unreddened star HD 188510 appears to be incorrect: the *Hipparcos* catalogue gives $\pi = 25.32 \pm 1.17$ mas for this star (instead of 22.80 mas), which implies that its M_V is 5.83 ± 0.10 , if $V = 8.83$ is taken to be its apparent magnitude and a Lutz-Kelker correction of -0.02 mag is applied.

in the case of HD 134439 and HD 134440, Clementini et al. (1999).⁸ As the α -elements appear to be overabundant by ~ 0.3 dex in the vast majority of field halo stars (see, e.g., the Clementini et al. study), the offsets in T_{eff} [and in $(B - V)_0$ color, to be discussed shortly] that were applied to the selected stars were derived from our isochrones for $[\alpha/\text{Fe}] = 0.3$, an age of 14 Gyr, and the range in $[\text{Fe}/\text{H}]$ between -2.31 and -1.14 . [With the exception of HD 132475, the locations of stars in Fig. 6 are nearly, or completely, independent of the age of the isochrones which are used to determine the offsets. Moreover, the position of HD 132475 remains indicative of high age (> 14 Gyr), irrespective of which isochrones are employed in this analysis.]

The main conclusion to be reached from Fig. 6 is that the theoretical and “observed” T_{eff} scales at $M_V > 5$ agree extremely well. This is very encouraging from our perspective because, as discussed in their paper, the Gratton et al. (1996) determinations of effective temperature are consistent with those derived from a number of methods — including the fitting of Balmer line profiles (e.g., Fuhrmann, Axer, & Gehren 1994), which is widely considered to be one of the more accurate techniques. It is interesting to note that HD 19445 is believed to have quite high oxygen and α -element abundances ($[\text{O}/\text{Fe}] = 0.56$ and $[\alpha/\text{Fe}] = 0.38$, according to Gratton et al. 1997), which may explain why this star sits to the right of the isochrones. On the other hand, it is puzzling that the locations of HD 134439 and HD 134440 are not discrepant, given that they are examples of the small minority of Population II field stars that apparently have $[\alpha/\text{Fe}] \approx 0$ (King 1997). However, we would not expect their displacements to hotter temperatures to be more than $\delta(\log T_{\text{eff}}) = 0.005\text{--}0.010$, judging from our models, and such small shifts are probably consistent with the uncertainties associated with the T_{eff} and $[\text{Fe}/\text{H}]$ determinations. (We have no explanation for the somewhat anomalous location of HD 145417 relative to the locus defined by the other subdwarfs.)

As illustrated in Figure 7, the same subdwarfs define a mono-metallicity sequence on the $[M_V, (B - V)_0]$ -plane that is also in good agreement with the same isochrones, when the predicted effective temperatures are converted to $B - V$ colors using very close to Bell & Gustafsson (1989) transformations (see Paper I for some discussion of the adopted color- T_{eff} relations). Thus, there is no obvious need to adjust either the temperatures or the colors of the models in order to satisfy the constraints posed by the subdwarf sample that has been considered. Granted, a couple of the stars (HD 25329, HD 188510) are slightly displaced from the theoretical loci in Fig. 7, but not in Fig. 6, which suggests that the adopted temperatures and colors are not perfectly consistent with one another. But this could simply be an indication that the reddenings of these two stars are slightly higher than the values adopted by Carretta et al. (2000). An underestimation of the reddenings of HD 134439 and HD 134440 could also explain why they sit on the same locus as HD 103095 despite the latter having $[\alpha/\text{Fe}] \approx 0.3$ (Gratton et al. 1997), and the former two stars

⁸Effective temperatures for HD 132475 and HD 145417 were kindly provided to us by Raffaele Gratton: they are, in turn, 5800 K and 4953 K.

having $[\alpha/\text{Fe}] \approx 0.0$, as already noted.

The other striking feature of Figs. 6 and 7 is that high ages are implied by the locations of the post-turnoff stars. As emphasized by Grundahl et al. (2000), HD 140283 provides an especially strong argument that there are very old stars and, furthermore, that the most metal-deficient globular clusters must be of comparable age if the local subgiants are representative of cluster subgiants of similar metal abundance. Indeed, Paper II has shown that excellent agreement between synthetic and observed C-M diagrams is obtained for such systems as M 92 if its age is ~ 16 Gyr. To be sure, there is sufficient flexibility in the Mixing Length Theory of convection to obtain good fits to the morphology of an observed C-M diagram for any assumed distance (within reason). But if M 92 is as young as 12 Gyr, say, then the zero-point of our adopted color– T_{eff} relations would require a large correction, in conflict with our findings from Figs. 6 and 7, and M 92 would be ~ 4 Gyr younger than field halo stars of similar $[\text{Fe}/\text{H}]$, which seems unlikely.

To elaborate on this point, we show in Figure 8 two fits of isochrones to the M 92 C-M diagram where the only difference in the models is the choice of α_{MLT} , the usual mixing-length parameter. The left-hand panel reproduces the same isochrones that were plotted in Fig. 7 and it is obvious that a superb match to the cluster fiducial is obtained if the adopted distance is near $(m - M)_V = 14.60$ and if $E(B - V) = 0.023$ mag (Schlegel, Finkbeiner, & Davis 1998). This case assumes a value of α_{MLT} that is needed to satisfy the solar constraint (see Paper I), and the distance is approximately what one would infer from HD 140283 if M 92 and the field subgiant are close to being coeval. However, even if the cluster distance modulus is actually as high as $(m - M)_V = 14.90$, it is still possible to obtain an equally fine fit to the *shape* of the observed C-M diagram simply by adopting $\alpha_{\text{MLT}} = 2.50$ (see the right-hand panel).⁹ The main problem with this scenario is that a very large correction must be applied to the model colors in order for the relevant isochrone (for an age of ≈ 12 Gyr) to match the observed turnoff color. Such a large color shift would seem to be precluded by the comparisons given in Figs. 6 and 7.

4.2. On the Globular Cluster and Subdwarf $[\text{Fe}/\text{H}]$ Scales

While Paper I and the present discussion appear to offer strong support for the T_{eff} and $[\text{Fe}/\text{H}]$ scales derived by Gratton et al. (1996) and Carretta et al. (2000) for the local subdwarfs, Paper II has suggested that the metallicities determined by Carretta & Gratton (1997) for globular clusters, especially those with $-2 \lesssim [\text{Fe}/\text{H}] \lesssim -1$, are too high. Something much closer to the Zinn & West

⁹Discrepancies do become evident at both brighter and fainter magnitudes than those plotted if the high value of α_{MLT} is assumed. Hence, in this instance, one may have to postulate some variation in the value of the mixing-length parameter with evolutionary state in order to match the entire C-M diagram. Of course, there is no reason why this parameter should be completely independent of T_{eff} and/or $\log g$, but it is interesting that no such difficulty is found if $\alpha_{\text{MLT}} = 1.89$.

(1984) scale was favored. Because this is such an unexpected (and controversial) result, some additional comments on this matter are worthwhile. In particular, if our inference from Figs. 6 and 7 is correct, that our isochrones require little or no adjustment of the predicted colors to match the local calibrators, then we should obtain reliable estimates of globular cluster distances by performing main-sequence fits of the cluster fiducials to our isochrones. Quite understandably, the results of such an exercise depend sensitively on what metal abundances are assumed.

This is illustrated in Figure 9, using M3 as an instructive example. Recall that Carretta & Gratton (1997) have determined $[\text{Fe}/\text{H}] = -1.34$ for this system whereas the Zinn & West (1984) estimate is -1.66 . Hence, the most appropriate isochrones in our grid to use in this analysis are those having $[\text{Fe}/\text{H}] = -1.31$ and -1.71 . If the Stetson et al. (1999) fiducial for M3 is fitted to the models of higher metallicity (see the left-hand panel), then one obtains $(m - M)_V = 15.17$ and an age of ≈ 10 Gyr. (A main-sequence fit to local subdwarfs will necessarily yield the same relatively young age for M3 if the cluster iron abundance is as high as the Carretta & Gratton estimate.) This is to be compared with $(m - M)_V = 14.95$ and an age of ≈ 14 Gyr if a fit is performed to the lower-metallicity isochrones (see the right-hand panel). [Our transformations to $V - I$ are precisely as given by Bell & Gustafsson (1989) and, as shown in Papers I and II, very similar interpretations of both cluster and subdwarf C-M diagrams are generally found regardless of whether the color used is $B - V$ or $V - I$.]

The isochrones for $[\text{Fe}/\text{H}] = -1.31$ clearly fail to match the morphology of the M3 fiducial whereas the predicted and observed loci agree extremely well if the assumed $[\text{Fe}/\text{H}]$ is -1.71 . By itself, this is not a particularly strong argument against the comparison shown in the left-hand panel of Fig. 9, given that isochrone shapes are so easily manipulated (as we have already demonstrated). A more compelling reason for rejecting this possibility is the fairly strong case that has been made in support of an age of ~ 16 Gyr for M92 and the finding that isochrones for this age, and a metallicity within the uncertainties of most determinations, do not require any *ad hoc* adjustments to either the model temperatures or colors to achieve nearly perfect coincidence with the cluster (and subdwarf) C-M diagrams. It seems highly improbable that M3 is 5–6 Gyr younger than M92 and that the isochrone fit would be so problematic for the one cluster, but not for the other. There are no such difficulties if the $[\text{Fe}/\text{H}]$ value obtained by Zinn & West (1984) for M3 is more realistic than that derived by Carretta & Gratton (1997).

This conclusion does depend on the accuracy of the assumed reddening and α -element abundances as well as, among other things, the photometric zero-points, so it may well be revised somewhat as further progress is made. However, it would not be too surprising if globular cluster abundances, as derived from spectroscopic data for the brightest giants, are not quite on the same scale as that of local field halo dwarfs. (Note that the age estimates discussed above should probably be reduced by about 10% to take into account the effects of diffusion, though current diffusive models are not without their difficulties: for some discussion of this point, see Grundahl

et al. 2000.¹⁰)

4.3. RGB Slopes and RGB Tip Magnitudes

Paper I has already shown that, both in zero-point and slope, the computed giant branches on the $(M_{\text{bol}}, \log T_{\text{eff}})$ -plane agree very well with the loci inferred for globular clusters from infrared photometry. Our intention here is merely to point out that reasonably good agreement between theory and observations is also found on the various C-M diagrams that can be constructed from $BV(RI)_C$ magnitudes. As an example, we show in Figure 10 how well our isochrones are able to reproduce the Da Costa & Armandroff (1990) fiducials for M 15, NGC 6752, NGC 1851, and 47 Tuc on the $[M_I, (V - I)_0]$ -diagram. In preparing this figure, we have adopted the reddenings derived by Schlegel et al. (1998), relations giving $E(V - I)$ and A_I as a function of $E(B - V)$ from Bessell, Castelli, & Plez (1998), and the distance moduli that were derived in Paper II; thus, the fiducials tabulated by Da Costa & Armandroff have been corrected to take the small differences in $E(B - V)$ and $(m - M)_V$ between their adopted parameters and ours into account. Although we have plotted the giant-branch segments of isochrones for certain ages, to be consistent with the assumed distances, the comparison is fairly independent of this choice. It should be noted, as well, that the implied metallicities of the four clusters are within 0.1 dex of the [Fe/H] values listed in the compilation of such data by Harris (1996).

At $[\text{Fe}/\text{H}] \lesssim -1.5$, the adopted transformations to $V - I$ are exactly as given by Bell & Gustafsson (1989), whereas some adjustment of their color- T_{eff} relations (only at low gravities) was required at higher metal abundances to achieve consistency between the theoretical and observed planes. These corrections were always to the red and they tended to be systematically larger at higher [Fe/H] values, which may indicate the lack of sufficient blanketing in the model atmospheres constructed by Bell & Gustafsson for cool, relatively metal-rich giants. In any case, it is desirable to force the *colors* of the upper giant branches to agree with those observed in order to enhance the usefulness of our models in stellar population studies. [Even though there are some discrepancies between the $[\text{Fe}/\text{H}] = -0.83$ isochrone and the 47 Tuc fiducial at the brightest magnitudes, this does not necessarily indicate a problem with the adopted color transformations. It may be, for

¹⁰After this paper was submitted for publication, a preprint became available which adds to the evidence that something inhibits the gravitational settling of heavy elements in at least the surface layers of very metal-deficient stars. Gratton et al. (2001) have found, from VLT high-dispersion spectroscopy, essentially no difference in the derived [Fe/H] values for large samples of turnoff and lower RGB stars in two globular clusters, NGC 6397 and NGC 6752. The failure to find any variation of [Fe/H] across the cluster subgiant branches, together with the unexpectedly high Li abundances found in both cluster (Molaro & Pasquini 1994) and field turnoff stars (e.g., Spite & Spite 1982, Swenson 1995), provide extremely important constraints on diffusion in Population II stars that have yet to be properly evaluated. It seems very likely that the age effect, which arises from the settling of helium in the deep interior, will persist, but the effective temperatures predicted by currently available diffusive models may well need to be revised significantly. A collaboration between the University of Montreal (G. Michaud and colleagues) and D.A.V. is underway to study this problem.

instance, that 47 Tuc has a slightly higher iron abundance, and given the huge sensitivity of the $V - I$ color index (as well as the bolometric corrections) to T_{eff} at low temperatures, a better fit to the upper end of the cluster fiducial would be obtained if either the predicted temperatures were reduced slightly or the adopted [Fe/H] value were increased by $\lesssim 0.1$ dex.]

In contrast to the colors, which were constrained to some extent to satisfy empirical data (for giants only), the bolometric corrections to V magnitudes do represent purely theoretical predictions (at all temperatures, gravities, and [Fe/H] values). In particular, we have adopted the bolometric corrections given by Wood & Bessell (1994), which are based on Kurucz model atmospheres and which span a very wide range in parameter space. They agree extremely well in a systematic sense with those computed recently by R.A. Bell (see, e.g., the discussion by VandenBerg & Irwin 1997). For instance, we have found that Bell’s transformation of selected isochrones to fit the M92 and NGC 2419 C-M diagrams in the study by Harris et al. (1997) is nearly indistinguishable with ours. Hence, a comparison of predicted and observed giant-branch tip magnitudes does provide a valid test of the theoretical models. (Bolometric corrections in I were obtained from $BC_I = BC_V + V - I$.)

Considering that cluster distance moduli are currently uncertain by at least 0.2 mag, the luminosity at which giant-branch evolution is predicted to terminate, and its variation with metallicity, is in satisfactory agreement with observations (see Fig. 10). If anything, slightly shorter distances, implying somewhat higher ages, may be indicated for M15 and NGC1851. It should be appreciated that the *bolometric* magnitudes for the giant-branch tip are within 0.05 mag of those predicted by A.V. Sweigart for stars of the same mass and chemical composition (see Paper I) and within ≈ 0.1 mag of those reported by e.g., Cassisi et al. (1998), when very similar physics is adopted. (Sweigart’s models are fainter than ours while those by Cassisi et al. are brighter.) As the same neutrino cooling rates have been used by the aforementioned investigators, we suspect that small differences in the respective equation-of-state formulations are responsible for the minor variations in the predicted tip magnitudes. This should be investigated further.¹¹

4.4. RGB Bump Magnitudes

Another important diagnostic in observed C-M diagrams is the luminosity on the red-giant branch where the H-burning shell in evolving stars passes through the chemical abundance discontinuity left behind when the convective envelope reached its maximum penetration (near the base of the RGB). When this occurs, the evolution up the giant branch either slows down or reverses direction for a short time as the structure of the star adjusts to a somewhat larger

¹¹We note that Ferraro et al. (2000) have recently presented extensive, high-quality JK photometry for the red-giant and horizontal-branch populations in 10 globular clusters. We hope to examine how well our models are able to reproduce their observations at some future date, once we have fully investigated the transformations to $V - K$ and $J - K$.

fuel supply (higher H abundance). This manifests itself as a local enhancement in the number of stars in an otherwise smoothly decreasing differential luminosity function for the giant-branch component of a populous system such as a globular cluster — where, with few exceptions (e.g., ω Cen), the member stars are essentially coeval and chemically homogeneous. As discussed by Cassisi & Salaris (1997, and references therein), the luminosity of this so-called “RGB bump” is a strong function of metallicity and age, and depends only weakly on other factors such as the helium abundance and the mix of heavy elements. However, one must be wary of placing too much reliance on this feature as a distance (and age) constraint, given the possibility that there may be some amount of overshooting below the convective envelope (e.g., Alongi et al. 1991), or that opacities in the critical $\sim 10^6$ K regime are still inadequate, or that oxygen abundances are much higher than we have assumed. (As shown in Paper I, oxygen is the dominant contributor to the opacity at $5.8 \lesssim \log T \lesssim 6.7$, and its abundance will therefore have important consequences for the depth of the envelope convection zones in giants; also see VandenBerg & Bell 2001).

Table 6 lists the bump magnitudes predicted by our models for ages from 10 to 16 Gyr and the entire range of [Fe/H] and $[\alpha/\text{Fe}]$ values considered in this investigation. The considerable sensitivity of M_V^{bump} to these three parameters is clearly evident, and a careful inspection of this table, in conjunction with Table 2 of Paper I (which gives the Z value for each mixture), reveals that the chemical composition dependence is primarily with Z , the total mass-fraction abundance of the elements heavier than helium. That is, the detailed distribution of the metals affects the results at only the level of a few to several hundredths of a magnitude. Compare, for instance, the tabulated magnitudes for $[\text{Fe}/\text{H}] = -2.31$ and $[\alpha/\text{Fe}] = 0.6$ ($Z = 3.07 \times 10^{-4}$) with those for $[\text{Fe}/\text{H}] = -1.84$ and $[\alpha/\text{Fe}] = 0.0$ ($Z = 3.0 \times 10^{-4}$): the differences in M_V^{bump} are $\lesssim 0.04$ mag. Only at relatively high values of Z do these differences rise to ≈ 0.1 mag; e.g., compare the tabulated magnitudes for $[\text{Fe}/\text{H}] = -1.31$ and $[\alpha/\text{Fe}] = 0.6$ ($Z = 3.07 \times 10^{-3}$) with those for $[\text{Fe}/\text{H}] = -0.83$ and $[\alpha/\text{Fe}] = 0.0$ ($Z = 3.0 \times 10^{-3}$).

At the same Z , the bump magnitudes predicted by our models agree quite well (generally to within 0.05 mag) with those reported by Cassisi & Salaris (1997, see their Table 1) and with those computed by Straniero, Chieffi, & Limongi (1997), as noted by Rood et al. (1999). (Some differences can be expected due to the fact that the different studies assume slightly different helium contents and heavy-element mixtures.) Thus, the interpretation of this feature in observed C-M diagrams should be nearly independent of whose models are used. Much more critical is the adopted metallicity. For instance, Rood et al. have found that our models for $[\text{Fe}/\text{H}] = -1.31$, $[\alpha/\text{Fe}] = 0.3$, and an age of ≈ 12 Gyr accurately predict the location of the RGB bump in M3 (as do the models by Salaris et al. for the same age and nearly the same Z , but with the metals in solar proportions). In this cluster, $V_{\text{bump}} = 15.45 \pm 0.05$ (Ferraro et al. 1999), and an age of 12 Gyr is obtained if the cluster distance modulus is close to $(m - M)_V = 15.03$, which implies $M_V^{\text{bump}} \approx 0.42$, in excellent agreement with the relevant entry in Table 6. However, as we have argued above, such a high metal abundance for M3 is problematic. Indeed, Rood et al. have found

that it is impossible to choose a distance and metallicity such that the corresponding models are able to reproduce the entire luminosity function (LF). In particular, they found that a good fit to the subgiant LF resulted in a poor fit to the luminosity of the RGB bump, and vice versa. An appreciably higher age ($\gtrsim 14$ Gyr), and/or a lower metallicity, is indicated by the slope of the LF between the turnoff and lower giant branch.

It is especially unfortunate that the chemical composition of M 3 is so uncertain at the present time: the $[\text{Fe}/\text{H}]$ values determined by Zinn & West (1984), Carretta & Gratton (1997), and Kraft et al. (1998, see their Table 6) differ from one another by $\gtrsim 0.15$ dex and span a range > 0.30 dex. Until these differences are understood, it will be difficult to say whether or not models accurately predict the observed bump magnitude in this cluster. However, it does seem unlikely that such a reconciliation of theory and observation is possible in the case of M 92, *if* it is older than ~ 12 Gyr. For this system, current metallicity determinations are much more consistent with one another — e.g., high-resolution spectroscopy of bright giants by Sneden et al. (1991) and Carretta & Gratton (1997) has yielded $[\text{Fe}/\text{H}] = -2.25$ and -2.16 , respectively, while Zinn & West give $[\text{Fe}/\text{H}] = -2.24$. Moreover, most spectroscopic studies seem to find $[\alpha/\text{Fe}] \approx 0.3$ for most globular clusters, including M 92 (see the spectroscopic studies mentioned above, as well as the reviews by Kraft 1994 and Carney 1996).¹²

As shown in Table 7, our models are able to match the luminosity of the RGB bump in M 92 only if the cluster metallicity is at the high end of the observed range and its age is $\lesssim 12$ Gyr. According to Ferraro et al. (1999), $V_{\text{bump}} = 14.65 \pm 0.05$ in M 92, which corresponds to the absolute visual magnitudes given in the fifth column if the distance moduli in the third column are assumed. At these distances, the ages obtained from our models and the corresponding bump luminosities (from Table 6) are as tabulated in the fourth and sixth columns, respectively. The last column, which contains the differences between the observed and predicted bump M_V^{bump} values, shows that the latter are too bright by 0.05 to 0.31 mag, depending on the distance and iron abundance that is assumed. In view of the fairly strong case that has been made in support of an age near 16 Gyr for M 92 (see §4.1 above, and Grundahl et al. 2000), we are inclined to conclude that the our models fail to predict the luminosity of the RGB bump in this cluster by at least 0.2 mag.

In fact, a very similar conclusion is reached from an analysis of the C-M diagram for 47 Tuc, which has $[\text{Fe}/\text{H}] \gtrsim -0.8$. It has $V_{\text{bump}} = 14.55 \pm 0.05$ mag (Ferraro et al. 1999), and if we adopt $(m - M)_V = 13.4$, which is within 0.1 mag of most estimates (and slightly higher than our preferred value: see Paper II), then $M_V^{\text{bump}} = 1.15$. At this distance, the age and bump magnitude

¹²Should it turn out that M 92 stars have $[\text{O}/\text{Fe}] \approx 1.0$ (Israelian et al. 1998, Boesgaard et al. 1999), then the cluster age could be as low as ~ 13 Gyr *and* there would be no discrepancy between the predicted and observed bump magnitudes (see VandenBerg & Bell 2001).

predicted by our isochrones for $[\text{Fe}/\text{H}] = -0.83$ and $[\alpha/\text{Fe}] = 0.3$ (Brown, Wallerstein, & Oke 1990) are ≈ 11 Gyr and 0.91 mag, respectively. The corresponding numbers for isochrones having $[\text{Fe}/\text{H}] = -0.71$ and the same α/Fe ratio (Carretta & Gratton 1997) are ≈ 10.5 Gyr and 1.00 mag. Thus, the discrepancy between the predicted and observed values of M_V^{bump} is, in turn, 0.24 and 0.15 mag. Although the agreement could be improved by adopting a larger distance, any age younger than ≈ 10 Gyr at these metallicities poses problems for other features in the observed C-M diagram. For instance, the subgiant branch in 47 Tuc has a gentle upward slope between the turnoff and lower RGB on the $[V, (B - V)]$ -diagram, while isochrones for ages $\lesssim 10$ Gyr predict that the variation in V across the subgiant branch is non-monotonic (see Fig. 34 in Paper II).

If our models truly are incapable of explaining the location of the RGB bump in both M 92 and 47 Tuc, then it seems unlikely that they would fare any better at intermediate metal abundances. That is, there is some basis for expecting that the bump luminosity in M 3 *should* be ~ 0.2 mag fainter than that predicted by the most appropriate isochrone in our grid. It turns out to be quite difficult to force such a discrepancy unless the cluster is more metal poor than $[\text{Fe}/\text{H}] = -1.3$. This becomes readily apparent when one considers Figure 11, which illustrates how well isochrones for $[\text{Fe}/\text{H}] = -1.31$ and $[\alpha/\text{Fe}] = 0.3$ are able to reproduce the M 3 C-M diagram, on the assumption of smaller distances than that derived from a main-sequence fit (see the left-hand panel of Fig. 9). To identify which isochrone has the same turnoff luminosity as the cluster, small offsets to the synthetic colors were applied (as indicated).¹³

Since $V_{\text{bump}} = 15.45$, the assumption of $(m - M)_V = 15.00$ and 14.85 imply that $M_V^{\text{bump}} = 0.45$ and 0.60 mag, respectively. The observed turnoff luminosities in these two cases are clearly very close to those predicted by 12 and 14 Gyr isochrones, for which the predicted bump magnitudes (see Table 6) are, in turn, 0.45 and 0.52 mag. Because of the substantial dependence of M_V^{bump} on age, the difference between the theoretical and observed bump luminosities varies relatively slowly with distance modulus. Thus, in order to obtain $\Delta M_V^{\text{bump}} \gtrsim 0.15$ mag, M 3 would have to be older than 16 Gyr, if it has $[\text{Fe}/\text{H}] \approx -1.3$ and $[\alpha/\text{Fe}] \approx 0.3$. But such a high age would imply that the isochrone colors need to be corrected blueward by > 0.06 mag in $V - I$, which is completely unacceptable. There is no such difficulty if a metallicity close to the Zinn & West (1984) estimate is assumed (see the right-hand panel of Fig. 9). Note, as well, how much better the isochrones for lower Z match the observed C-M diagram. Interestingly, the 14 Gyr isochrone for $[\text{Fe}/\text{H}] = -1.31$ and $[\alpha/\text{Fe}] = 0.3$ is able to reproduce both the location of the main sequence and the RGB, once

¹³The fact that we need to shift the isochrones to the blue is itself suggestive that M 3 has a lower $[\text{Fe}/\text{H}]$, because little or no adjustment to the model colors seems to be necessary to match the properties of the local subdwarfs (as discussed above and in Paper I). However, as noted in Paper II (see Fig. 12 therein), the three best photometric data sets currently available for M 3 have zero-points that differ by up to ≈ 0.015 mag in $V - I$: the Stetson et al. (1999) fiducial, which we have used, is the bluest, while those by Johnson & Bolte (1998) and Rood et al. (1999) are redder. Had we used either of the latter, the offsets applied to the isochrones in Fig. 11 would have been smaller in an absolute sense by 0.01–0.015 mag (and a smaller distance moduli by ~ 0.08 mag would have been derived in Fig. 9). The accuracy of photometric zero-points is obviously an important concern in the main-sequence fitting technique.

a large zero-point adjustment is applied to the synthetic colors, but not the slope of the subgiant branch (see the right-hand panel of Fig. 11). Here is an example where it would not be possible to match the entire C-M diagram, if $(m - M)_V = 14.85$, simply by assuming a different value of α_{MLT} in the construction of the isochrones: there would have to be at least two things wrong with the models. All things considered, the $[\text{Fe}/\text{H}]$ value determined by Carretta & Gratton (1997) for M3 seems to be too high. [Even the somewhat higher value obtained by the Lick-Texas group from high-resolution spectroscopy of bright M3 giants (i.e., $[\text{Fe}/\text{H}] = -1.47$, Kraft et al. 1998) would seem to be too high by 0.1–0.2 dex according to the present analysis.]

We conclude this section with Figure 12, which plots the M_V^{bump} versus $[\text{Fe}/\text{H}]$ relations given in Table 6 for the $[\alpha/\text{Fe}] = 0.3$ case. Superimposed on this diagram are the predicted and observed bump magnitudes for M92, M3, M5, and 47 Tuc on the assumption of $[\text{Fe}/\text{H}]$ values that are within 0.1 dex of those given by Zinn & West (1984) and which present relatively few difficulties for our models. We have also adopted fairly high ages for these clusters, as indicated by the location of the *open circles* relative to the *solid curves*. This is for the following reason. Paper II found that, when zero-age horizontal branch loci are used to set the globular cluster distance scale, there was a significant dependence of mean age with metallicity. To be specific, the mean age varied smoothly from ≈ 14 Gyr at $[\text{Fe}/\text{H}] = -2.3$ to ≈ 11.5 Gyr at $[\text{Fe}/\text{H}] = -0.8$. However, it was also noted that this relation should be displaced to higher ages if the distances are set instead according to empirical determinations of the luminosities of RR Lyrae stars from, e.g., Baade-Wesselink and statistical parallax studies. As argued therein and in the present investigation, the short distance scale is also implied by field Population II subdwarfs and subgiants.

Thus, in order to satisfy other constraints, we conclude that our models fail to match the observed luminosities of the RGB bump in clusters by ≈ 0.25 mag. This is certainly speculation on our part, but not without justification. The location of radiative–convective boundaries in stars is subject to a lot of uncertain physics and it would not be too surprising that current models are somewhat lacking in this regard. Whether or not the scenario that we have described is realistic may be difficult to confirm or refute until the uncertainties associated with current distance, T_{eff} , and chemical abundance determinations are significantly reduced.

5. Concluding Remarks

The algorithms presented in BV92 to produce isochrones, LFs, and CFs from grids of evolutionary sequences have been improved with the implementation of the Akima spline to replace linear interpolation. Experiments with the interpolating algorithms show that they work well, over a wide range in metallicity ($+0.12 \geq [\text{Fe}/\text{H}] \geq -2.31$) and ages (from ~ 1 Gyr, which is the youngest age that has been examined, to 20 Gyr), to produce the morphology of isochrones accurately. Moreover, what we have called the “isochrone population function”, which literally gives the number of stars at any location along the corresponding isochrone, has been built into the interpolation algorithms.

Software (FORTRAN 77) has been developed to implement the algorithms for grids of evolutionary sequences with $-2.31 \leq [Fe/H] \leq -0.30$. Each grid of sequences is available with three α -element enhancements: $[\alpha/Fe] = 0.0, +0.3$, and $+0.6$. [Note that the diffusion of helium and heavy elements has not been treated in the models. However, as mentioned at the end of section 4.2 (also see Grundahl et al. 2000), current observations of Population II stars appear to be inconsistent with the predictions of diffusive models (like those recently reported by Salaris, Groenewegen, & Weiss 2000), for reasons that have yet to be understood.] The evolutionary grids, together with the software are available to the astronomical community, so that users can generate isochrones, IPFs, LFs, and CFs for the particular set of abundances and ages of interest to them.

The IPF is a particularly powerful tool for stellar astrophysics and for stellar population studies because it contains all of the information found in isochrones, LFs, and CFs in a compact form. For example, magnitudes and color indices for synthetic stellar populations can easily be generated from the cumulative form of the IPF for any pair of B , V , R , and I , for which empirically constrained color– T_{eff} relations and bolometric corrections are supplied as part of the package. (Transformations to the Strömgren system, presently being developed by J. Clem at the University of Victoria, will be provided in the near future. Those involving the JHK , and possibly U , bands will be added at a later date.) A side benefit of the differential IPFs, LFs, and CFs is that they provide a way of fine tuning the transformation tables that are used to transpose the models from the $\log L$ – $\log T_{\text{eff}}$ plane to the observer’s plane.

The additional tests of the models that we have carried out to augment those described in Papers I and II suggest that the computed temperatures and adopted color– T_{eff} relations are quite realistic. The apparent agreement between the predicted and observed properties of local subdwarfs having well-determined parallaxes ($\sigma_{\pi}/\pi \lesssim 0.1$, as measured by *Hipparcos*) is especially encouraging. Indeed, there should be no difference between the distances which are derived to e.g., globular star clusters when the observed fiducials are fitted either to the subdwarf calibrators or to our theoretical isochrones. However, in practice, the large uncertainty that presently exists in the GC [Fe/H] scale (see, e.g., Rutledge, Hesser, & Stetson 1997) is a severe limitation of the main-sequence fitting technique. Be that as it may, it is our impression that something close to the Zinn & West (1984) scale is required to achieve the best overall consistency between synthetic and observed CMDs (and between distance estimates based on the subdwarf and RR Lyrae “standard candles” — see Paper II).

Both in zero-point and in slope, and on either the theoretical or observed planes, our computed giant branches agree well with those derived observationally. The models do not reproduce the luminosity of the RGB bump as well as they should, but this may simply be an indication that there is some overshooting of the convective envelopes of red giants into their radiative interiors — as suggested some time ago by, e.g., the Padova group (Alongi et al. 1991). In conclusion, we believe that the present grid of models is particularly well constrained and it should provide a valuable tool for the interpretation of stellar data, whether through the fitting of isochrones, LFs, and CFs or through the construction of integrated stellar population models whose properties can

be compared with those of distant systems.

We thank Raffaele Gratton for providing his estimates of the effective temperatures for a few field halo stars. The support of Operating Grants (to P.A.B. and to D.A.V.) from the Natural Sciences and Engineering Research Council of Canada is also gratefully acknowledged.

REFERENCES

Akima, H. 1970, Journal of the Association for Computing Machinery, 17, 589

Alongi, M., Bertelli, G., Bressan, A., & Chiosi, A. 1991, A&A, 244, 95

Alonso, A., Arribas, S., & Martínez-Roger, C. 1996, A&AS, 117, 227

Balachandran, S.C., & Carney, B.W. 1996, AJ, 111, 946

Bell, R.A., & Gustafsson, B. 1989, MNRAS, 236, 653

Bergbusch, P.A., & VandenBerg, D.A. 1992, ApJS, 81, 163 BV92

Bergbusch, P.A., & VandenBerg, D.A. 1997, AJ, 114, 2604

Bessell, M.S., Castelli, F., & Plez, B. 1998, A&A, 333, 231

Boesgaard, A.M., King, J.R., Deliyannis, C.P., & Vogt, S.S. 1999, AJ, 117, 492

Bolte, M. 1994, ApJ, 431, 223

Brown, J.A., Wallerstein, G., & Oke, J.B. 1990, AJ, 100, 1561

Brown, J.A., Wallerstein, G., & Zucker, D. 1997, AJ, 114, 180

Carretta, E., & Gratton, R.G. 1997, A&A, 121, 95

Carretta, E., Gratton, R.G., Clementini, G., & Fusi Pecci, F. 2000, ApJ, 533, 215

Carney, B.W. 1996, PASP, 108, 900

Cassisi, S., Castellani, V., Degl'Innocenti, S., & Weiss, A. 1998, A&A, 129, 267

Cassisi, S., & Salaris, M. 1997, MNRAS, 285, 593

Clementini, G., Gratton, R.G., Carretta, E., & Sneden, C. 1999, MNRAS, 302, 22

Da Costa, G.S., & Armandroff, T.E. 1990, AJ, 100, 162

Eggleton, P.P. 1971, MNRAS, 151, 351

Ferraro, F.R., Messineo, M., Fusi Pecci, F., De Palo, M.A., Straniero, O., Chieffi, A., & Limongi, M. 1999, AJ, 118, 1738

Ferraro, F.R., Montegriffo, P., Origlia, L., & Fusi Pecci, F. 2000, AJ, 119, 1282

Fuhrmann, K., Axer, M., & Gehren, T. 1994, A&A, 285, 585

Fulbright, J.P., & Kraft, R.P. 1999, AJ, 118, 527

Gratton, R.G., Bonifacio, P., Bragaglia, A., et al. 2001, astro-ph/0012457

Gratton, R.G., Carretta, E., & Castelli, F. 1996, A&A, 314, 191

Gratton, R.G., Fusi Pecci, F., Carretta, E., Clementini, G., Corsi, C.E., & Lattanzi, M. 1997, ApJ, 491, 749

Grundahl, F., VandenBerg, D.A., Bell, R.A., Andersen, M.I., & Stetson, P.B., 2000, AJ, submitted

Harris, W.E. 1996, AJ, 112, 1487

Harris, W.E., Bell, R.A., VandenBerg, D.A., et al. 1997, AJ, 114, 1030

Israelian, G., Garcia Lopez, R.J., & Rebolo, R. 1998, ApJ, 507, 855

Jimenez, R. & Padoan, P. 1998, ApJ, 498, 704

Johnson, J.A., & Bolte, M. 1998, AJ, 115, 693

King, J.R. 1993, AJ, 106, 1206

King, J.R. 1997, AJ, 113, 2302

Kraft, R.P. 1994, PASP, 106, 553

Kraft, R.P., Sneden, C., Smith, G.H., Shetrone, M.D., & Fulbright, J. 1998, AJ, 115, 1500

McWilliam, A. 1997, ARA&A, 35, 503

Molaro, P., & Pasquini, L. 1994, A&A, 281, L77

Nissen, P.E., & Schuster, W.J. 1997, A&A, 326, 751

Padoan, P. & Jimenez, R. 1997, ApJ, 475, 580

Renzini, A., & Fusi Pecci, F. 1988, ARA&A, 26, 199

Rood, R.T., Carretta, E., Paltrinieri, B., et al. 1999, ApJ, 523, 752

Rutledge, G.A., Hesser, J.E., & Stetson, P.B. 1997, PASP, 109, 907

Salaris, M., Groenewegen, M.A.T., & Weiss, A. 2000, A&A, 355, 299

Schlegel, D.J., Finkbeiner, D.P., & Davis, M. 1998, ApJ, 500, 525

Sneden, C., Kraft, R.P., Prosser, C.F., & Langer, G.E. 1991, AJ, 102, 2001

Spite, F., & Spite, M. 1982, A&A, 115, 357

Swenson, F.J. 1995, ApJ, 438, L87

Stetson, P.B., Bolte, M., Harris, W.E., et al. 1999, AJ, 117, 247

Straniero, O., Chieffi, A., & Limongi, M. 1997, ApJ, 490, 425

VandenBerg, D.A. 1992, ApJ, 391, 685

VandenBerg, D.A. 2000, ApJS, 129, 315 (Paper II)

VandenBerg, D.A., & Bell, R.A. 2001, New Astron. Rev., in press

VandenBerg, D.A., Bolte, M., & Stetson, P.B. 1990, AJ, 100, 445

VandenBerg, D.A., & Irwin, A.W. 1997, in Advances in Stellar Evolution, eds. R.T. Rood & A. Renzini (Cambridge: Cambridge Univ. Press), p. 22

VandenBerg, D.A., Swenson, F.J., Rogers, F.J., Iglesias, C.A., & Alexander, D.R. 2000, ApJ, 532, 430 (Paper I)

Wheeler, J.C., Sneden, C., & Truran, J.W., Jr. 1989, ARA&A, 27, 279

Wood, P.R., & Bessell, M.S. 1994, private communication by anonymous *ftp*

Zinn, R., & West, M.J. 1984, ApJS, 55, 45

Table 1: Evolutionary Track (EEP) File Format and Contents

Table 2: Isochrone (ISO) File Format and Contents

ISOCHRONES	6
[Fe/H]	-0.525
[alpha/Fe]	+0.3
Z	1.010D-02 Z = 6.000D-03 + alpha-element enhancement
X	0.742900
Y	0.247000
ALPHA(mlt)	1.89
Age	Npts
8.0	256
1	-1.333304 3.593967 0.5068505908 0.0000000 4.4097889D-01 4.2796556D-01
2	-1.285759 3.594365 0.5313098653 0.0595653 3.7309103D-01 3.6969990D-01
3	-1.236702 3.596696 0.5532147760 0.1251682 2.9388266D-01 3.0552844D-01
4	-1.187757 3.600882 0.5724189213 0.1992959 2.2815211D-01 2.4122070D-01
5	-1.140842 3.606441 0.5888593464 0.2801004 1.8235053D-01 1.9184230D-01
.	.
.	.
.	.
256	3.408755 3.529098 1.0791668980 7.7891261 2.0186710D-04 1.5983838D-04
Age	Npts
10.0	253
1	-1.339361 3.594616 0.5002053380 0.0000000 4.5027950D-01 4.5082604D-01
2	-1.299791 3.594533 0.5213256448 0.0494690 3.9824028D-01 3.9623085D-01
3	-1.258991 3.595736 0.5405685847 0.1018699 3.3393240D-01 3.3839995D-01
4	-1.217881 3.598282 0.5578690324 0.1592193 2.7157814D-01 2.8065268D-01
5	-1.177527 3.601987 0.5732006971 0.2218015 2.2171010D-01 2.3005911D-01
.	.
.	.
.	.
.	.

Table 3: Isochrone Probability Function (IPF) File Format and Contents

Table 4: Luminosity Function (LF) File Format and Contents

LFS	6	I	V-I	x = -0.5	+0.5	+1.5
[Fe/H]	-0.525					
[alpha/Fe]	+0.3					
Z	1.010D-02		Z = 6.000D-03 + alpha-element enhancement			
X	0.742900					
Y	0.247000					
ALPHA(mlt)	1.89					
Age	Npts					
8.0	57					
		I	x = -0.5	x = +0.5	x = +1.5	
1	7.200	4.54403	5.00000	4.68367	5.00000	4.80591
2	7.000	4.46666	4.96849	4.58374	4.95591	4.68324
3	6.800	4.43036	4.94023	4.52787	4.91738	4.60780
4	6.600	4.32834	4.91252	4.40940	4.88043	4.47284
5	6.400	4.27108	4.88928	4.33876	4.85003	4.38882
.
.
.
56	-3.800	1.17235	0.73334	1.02008	0.58107	0.85016
57	-3.982	1.17301	0.38695	1.02073	0.23467	0.85081
Age	Npts					
10.0	57					
		I	x = -0.5	x = +0.5	x = +1.5	
1	7.200	4.59146	5.00000	4.71916	5.00000	4.83211
2	7.000	4.51210	4.96470	4.61695	4.95194	4.70681
3	6.800	4.47533	4.93293	4.56047	4.90980	4.63058
4	6.600	4.36671	4.90154	4.43538	4.86909	4.48901
5	6.400	4.30264	4.87542	4.35813	4.83585	4.39858
.
.
.
.

Table 5: Color Function (CF) File Format and Contents

CFS	6	I	V-I	x = -0.5	+0.5	+1.5
[Fe/H]	-0.525					
[alpha/Fe]	+0.3					
Z	1.010D-02		Z = 6.000D-03 + alpha-element enhancement			
X	0.742900					
Y	0.247000					
ALPHA(mlt)	1.89					
Age	Npts	Nms				
8.0	177	53				
			V-I	x = -0.5	x = +0.5	x = +1.5
1	1.661	6.15467	5.00000	6.31226	5.00000	6.44939
2	1.650	5.48941	4.98464	5.62727	4.97775	5.74506
3	1.630	5.16197	4.95595	5.28373	4.93716	5.38481
4	1.610	4.96835	4.94176	5.08033	4.91742	5.17185
5	1.590	4.85784	4.93242	4.96383	4.90460	5.04942
.
.
.
52	0.650	5.54940	4.26728	5.42737	4.12937	5.28500
53	0.640	6.23807	4.05760	6.10449	3.90953	5.95048
54	0.640	6.23139	4.01804	6.09502	3.86857	5.93823
55	0.650	5.20946	3.97522	5.06719	3.82436	4.90450
.
.
.
176	3.070	1.11244	-0.39442	0.94847	-0.55839	0.76407
177	3.085	1.12639	-0.84117	0.96242	-1.00514	0.77801
Age	Npts	Nms				
10.0	179	50				
			V-I	x = -0.5	x = +0.5	x = +1.5
1	1.649	5.78583	5.00000	5.92022	5.00000	6.03681
2	1.630	5.24754	4.95007	5.35566	4.93044	5.44625
3	1.610	5.06810	4.93249	5.16642	4.90668	5.24674
4	1.590	4.88341	4.92045	4.97514	4.89059	5.04888
5	1.570	4.81476	4.91240	4.90146	4.87991	4.97015
.
.
.
.

Table 6. Predicted Magnitudes of the RGB Bump as a Function of Age and Chemical Composition

t(Gyr):		10	12	14	16	t(Gyr):		10	12	14	16
[Fe/H]	[α /Fe]	M_V^{bump}				[Fe/H]	[α /Fe]	M_V^{bump}			
-2.31	0.00	-0.59	-0.50	-0.43	-0.35	-2.14	0.00	-0.48	-0.39	-0.31	-0.23
	0.30	-0.46	-0.38	-0.30	-0.23		0.30	-0.34	-0.25	-0.18	-0.11
	0.60	-0.31	-0.23	-0.16	-0.10		0.60	-0.17	-0.09	-0.03	+0.03
-2.01	0.00	-0.41	-0.31	-0.22	-0.14	-1.84	0.00	-0.31	-0.21	-0.13	-0.06
	0.30	-0.27	-0.18	-0.10	-0.02		0.30	-0.13	-0.05	+0.03	+0.10
	0.60	-0.08	+0.01	+0.09	+0.15		0.60	+0.07	+0.16	+0.23	+0.29
-1.71	0.00	-0.19	-0.10	-0.03	+0.04	-1.61	0.00	-0.12	-0.03	+0.07	+0.13
	0.30	-0.02	+0.05	+0.13	+0.19		0.30	+0.06	+0.15	+0.22	+0.29
	0.60	+0.16	+0.25	+0.34	+0.42		0.60	+0.28	+0.36	+0.43	+0.50
-1.53	0.00	-0.05	+0.05	+0.12	+0.19	-1.41	0.00	+0.08	+0.17	+0.25	+0.31
	0.30	+0.13	+0.21	+0.28	+0.34		0.30	+0.26	+0.35	+0.42	+0.48
	0.60	+0.34	+0.43	+0.51	+0.58		0.60	+0.45	+0.54	+0.63	+0.71
-1.31	0.00	+0.15	+0.25	+0.34	+0.41	-1.14	0.00	+0.31	+0.41	+0.51	+0.59
	0.30	+0.36	+0.45	+0.52	+0.59		0.30	+0.54	+0.64	+0.71	+0.76
	0.60	+0.58	+0.66	+0.74	+0.81		0.60	+0.77	+0.86	+0.94	+1.00
-1.01	0.00	+0.45	+0.54	+0.63	+0.71	-0.83	0.00	+0.67	+0.77	+0.84	+0.91
	0.30	+0.69	+0.78	+0.84	+0.90		0.30	+0.87	+0.95	+1.02	+1.09
	0.60	+0.91	+1.01	+1.09	+1.16		0.60	+1.11	+1.20	+1.28	+1.34
-0.71	0.00	+0.79	+0.88	+0.95	+1.02	-0.61	0.00	+0.91	+1.01	+1.08	+1.14
	0.30	+0.98	+1.08	+1.18	+1.25		0.30	+1.10	+1.20	+1.29	+1.36
	0.60	+1.24	+1.34	+1.42	+1.49		0.60	+1.34	+1.43	+1.50	+1.58
-0.53	0.00	+0.99	+1.09	+1.18	+1.25	-0.40	0.00	+1.13	+1.23	+1.32	+1.39
	0.30	+1.21	+1.30	+1.37	+1.44		0.30	+1.34	+1.44	+1.52	+1.59
	0.60	+1.42	+1.52	+1.60	+1.67		0.60	+1.54	+1.65	+1.73	+1.80
-0.30	0.00	+1.26	+1.34	+1.40	+1.48						
	0.30	+1.44	+1.52	+1.59	+1.66						
	0.60	+1.65	+1.75	+1.81	+1.87						

Table 7. Comparison of the Observed and Predicted RGB Bump Magnitudes in M 92

[Fe/H]	$[\alpha/\text{Fe}]$	$(m - M)_V$	t(Gyr)	$M_{V,\text{obs}}^{\text{bump}}$	$M_{V,\text{theory}}^{\text{bump}}$	ΔM_V^{bump}
-2.31	0.30	14.90	12	-0.25	-0.38	+0.13
		14.70	14	-0.05	-0.30	+0.25
		14.57	16	+0.08	-0.23	+0.31
-2.14	0.30	14.85	12	-0.20	-0.25	+0.05
		14.67	14	-0.02	-0.18	+0.16
		14.54	16	+0.11	-0.11	+0.22

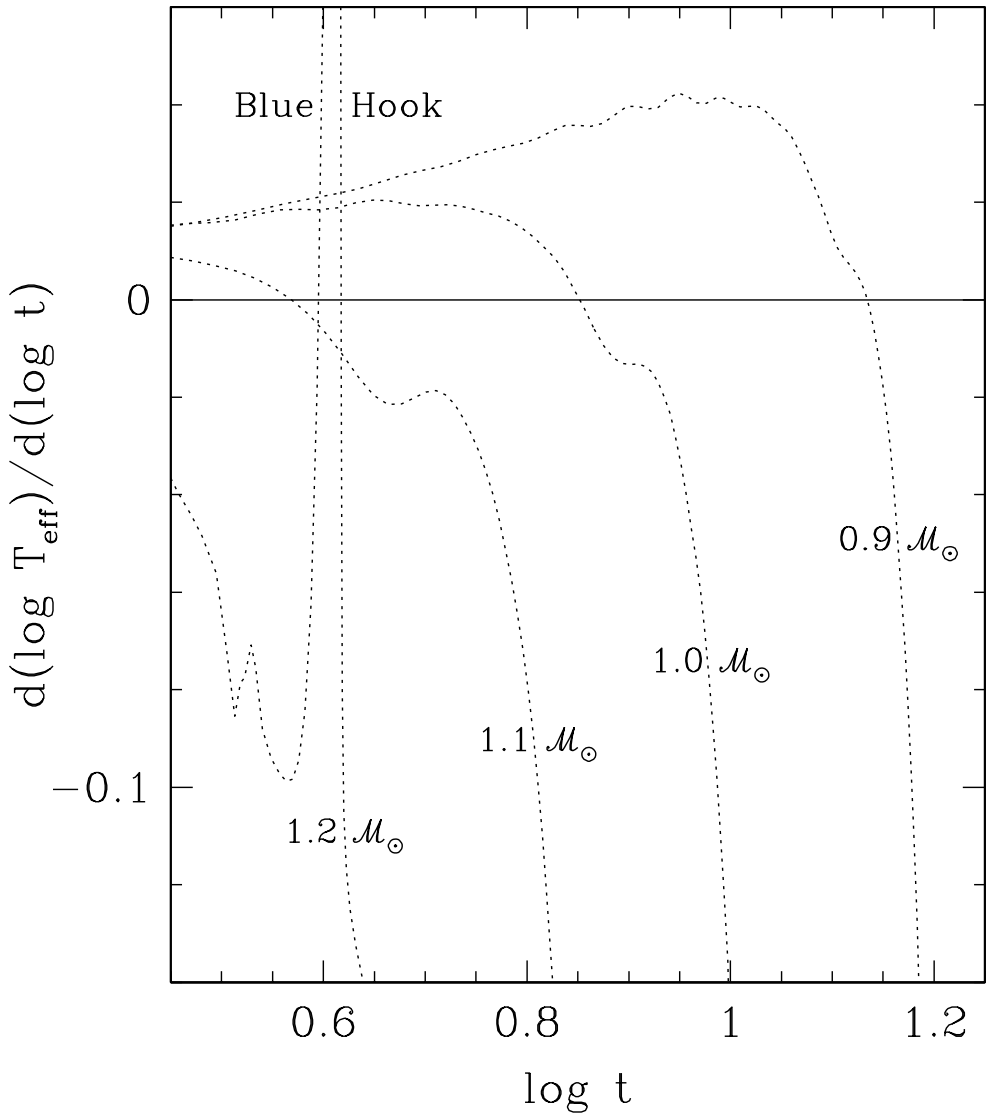


Fig. 1.— The derivative of T_{eff} with respect to time in the region of the turnoff is plotted for selected evolutionary tracks from a grid of models for $[\text{Fe}/\text{H}] = 0.0$. The blue hook in the $1.2 M_{\odot}$ track, which manifests itself as a spike in this derivative, occurs at an age which is somewhat greater than that of the turnoff point [where $d(\log T_{\text{eff}})/d(\log t) = 0.0$] in the $1.1 M_{\odot}$ track. To ensure that the age–mass relation remains monotonic, the small dip after the turnoff point in the 1.1 and $1.0 M_{\odot}$ tracks is used to define the second primary EEP.

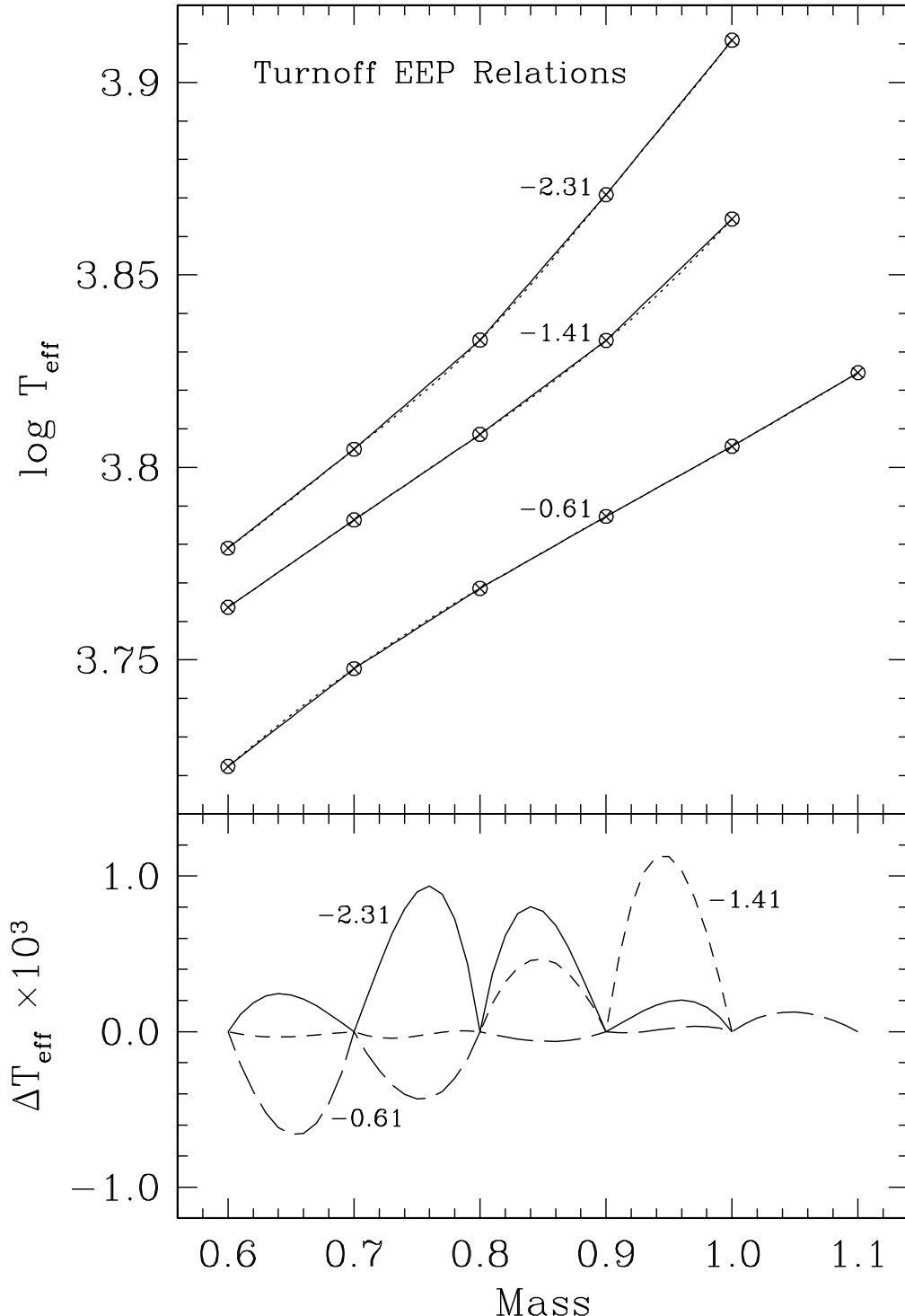


Fig. 2.— In the upper panel, the T_{eff} EEP relations at the turnoff (the second primary EEP) are plotted for the metallicities indicated from the $[\alpha/\text{Fe}] = 0.0$ grid of models. For each metallicity, the Akima spline fit is plotted as a *dotted curve*; linear interpolation is indicated by the *solid curve*. Differences between the relations, in the sense [linear] – [Akima] are plotted in the lower panel; the $[\text{Fe}/\text{H}] = -2.31$ differences are indicated by the *solid curves*, those for $[\text{Fe}/\text{H}] = -1.41$ by the *short-dashed curves*, and those for $[\text{Fe}/\text{H}] = -0.61$ by *long-dashed curves*.

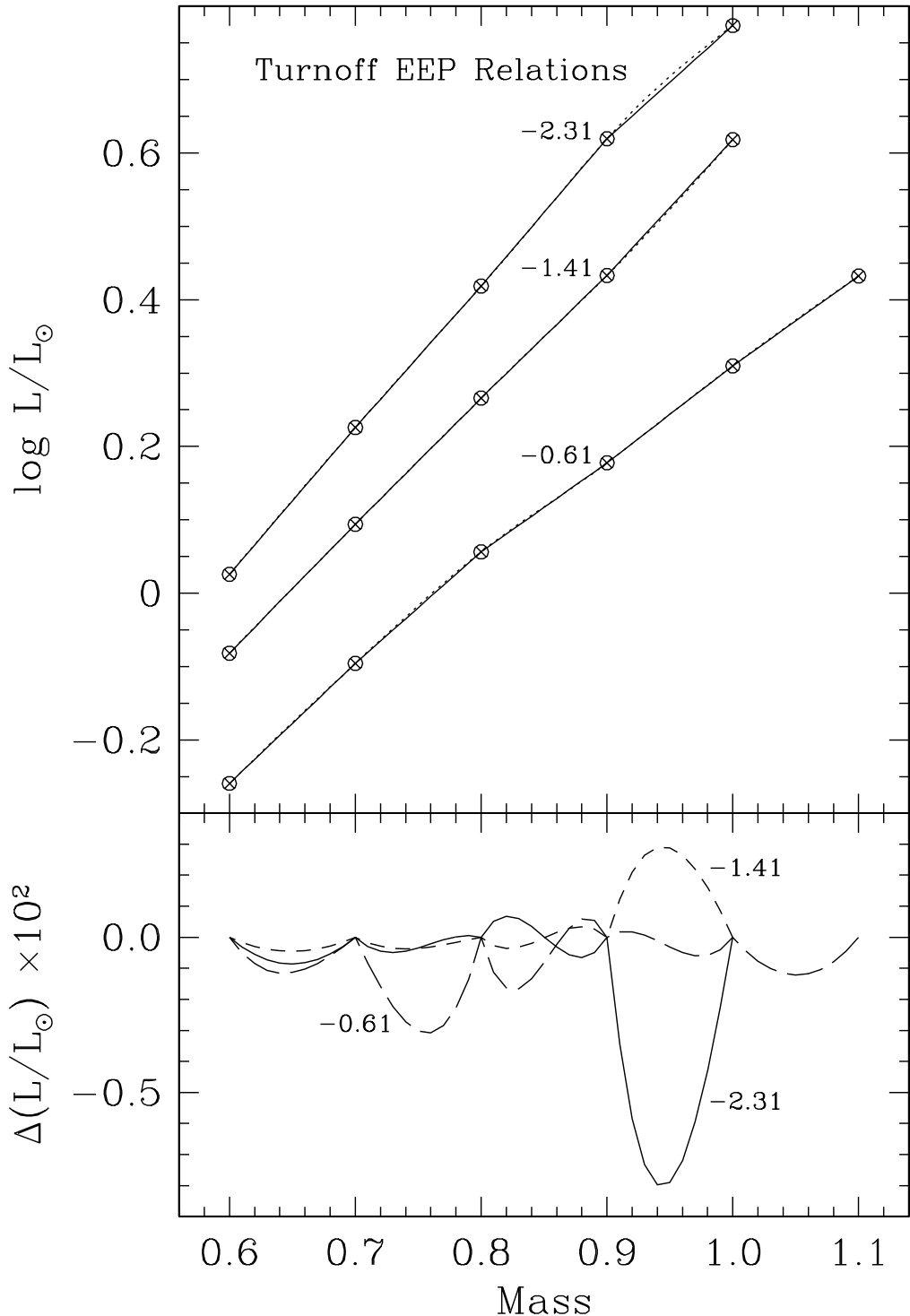


Fig. 3.— Similar to Fig. 2, except the luminosity EEP relations are plotted in the upper panel; the differences between the linear and Akima spline versions of the relations are plotted in the lower panel.

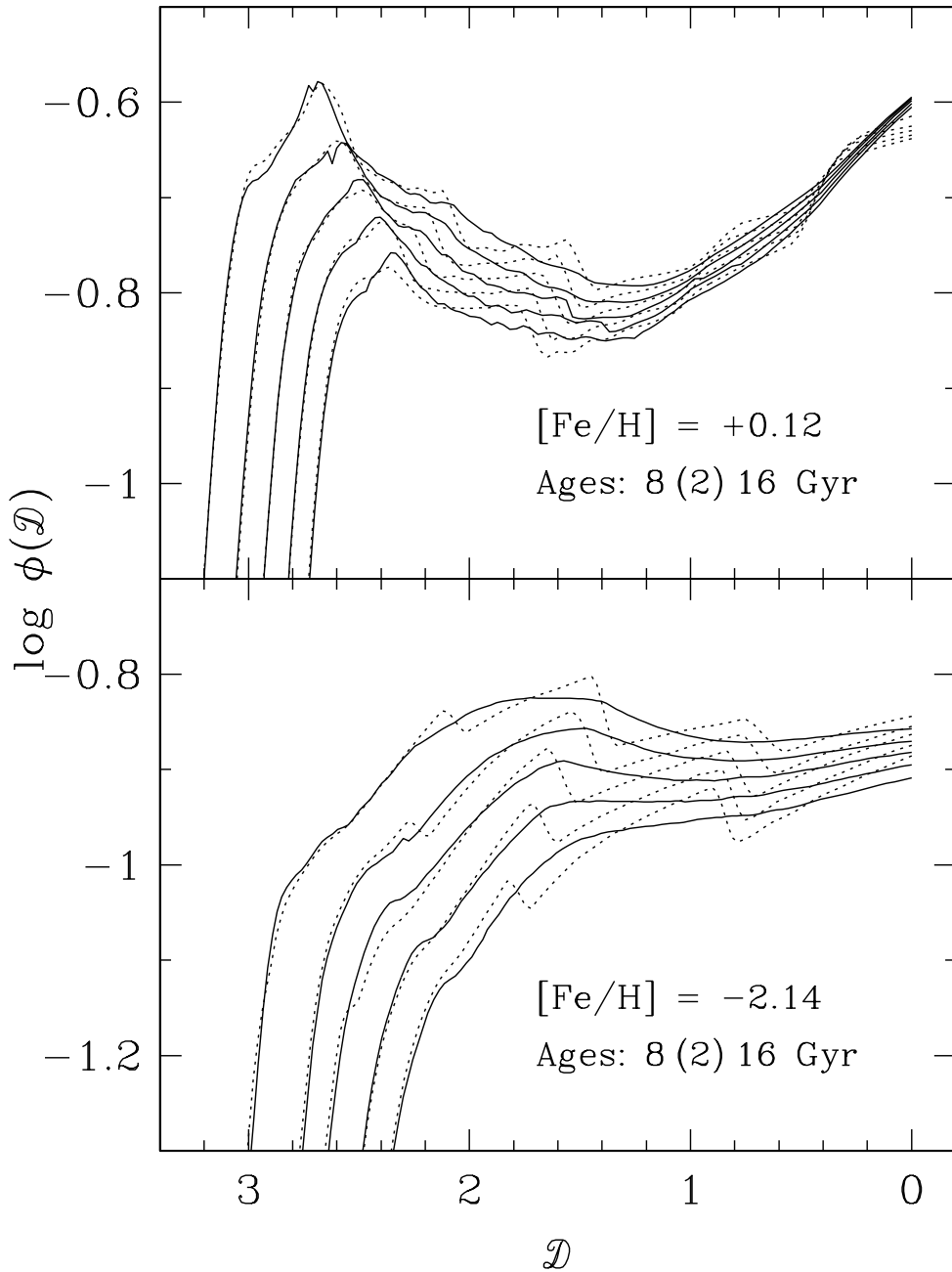


Fig. 4.— Differential IPFs on the theorist’s plane from the main sequence through the turnoff are plotted for the abundances and ages indicated. Those obtained from Akima spline interpolation, are plotted as *solid curves*; the corresponding IPFs obtained via purely linear interpolation are plotted as the *dotted lines*. On the theorist’s plane, the zero-point of *distance along an isochrone* is arbitrarily defined at the lowest mass point ($\approx 0.5M_{\odot}$).

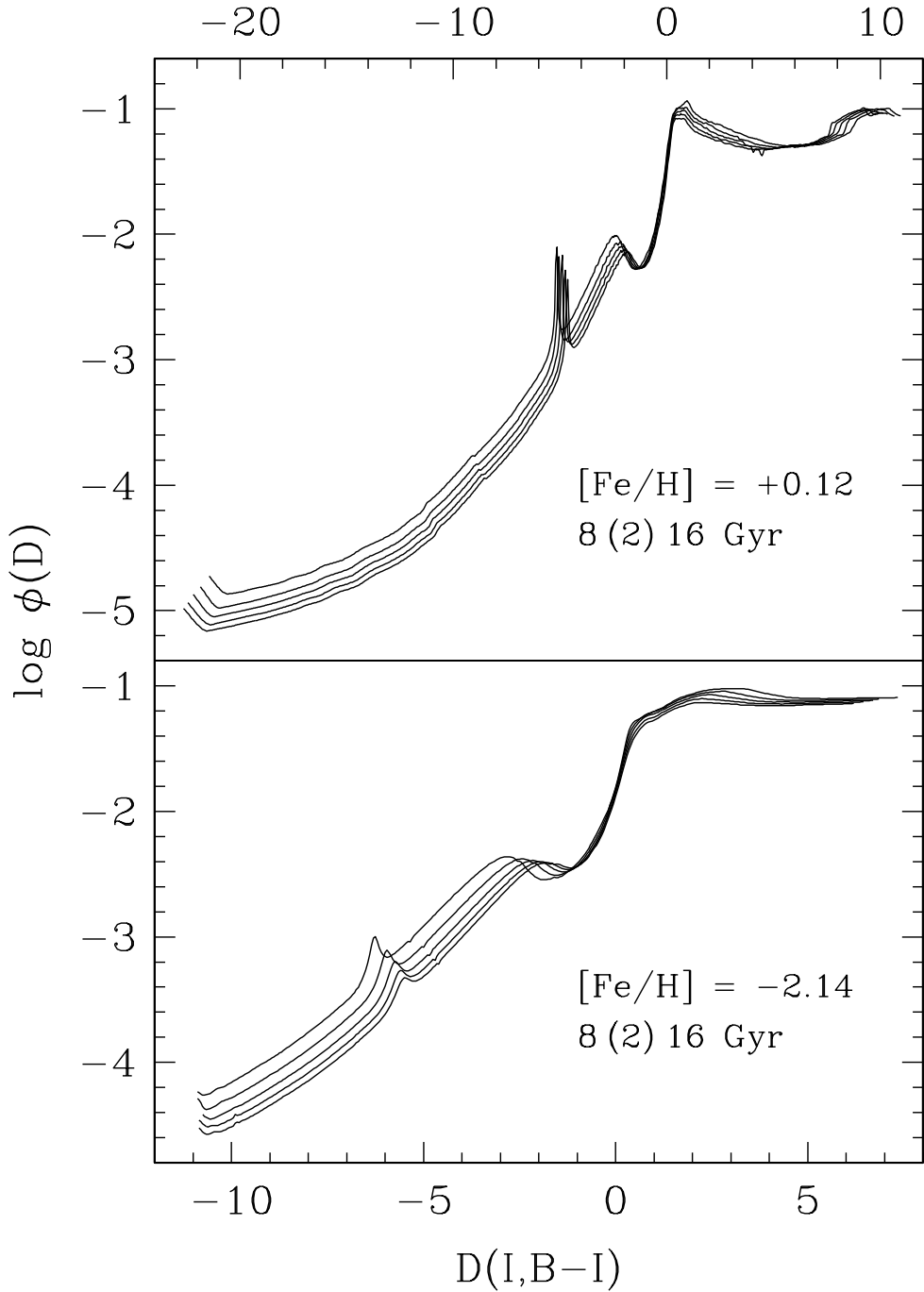


Fig. 5.— Differential IPFs in 0.05 mag distance bins are plotted as a function of distance on the $I-(B-I)$ observer's plane. The very small wiggles on the lower giant branch portions of these IPFs can be traced back to the evolutionary tracks; the larger, box-like structures seen on the main sequence and upper giant branch of the $[Fe/H] = +0.12$ models are artifacts produced by the color-temperature transformations and by the bolometric corrections which have been applied.

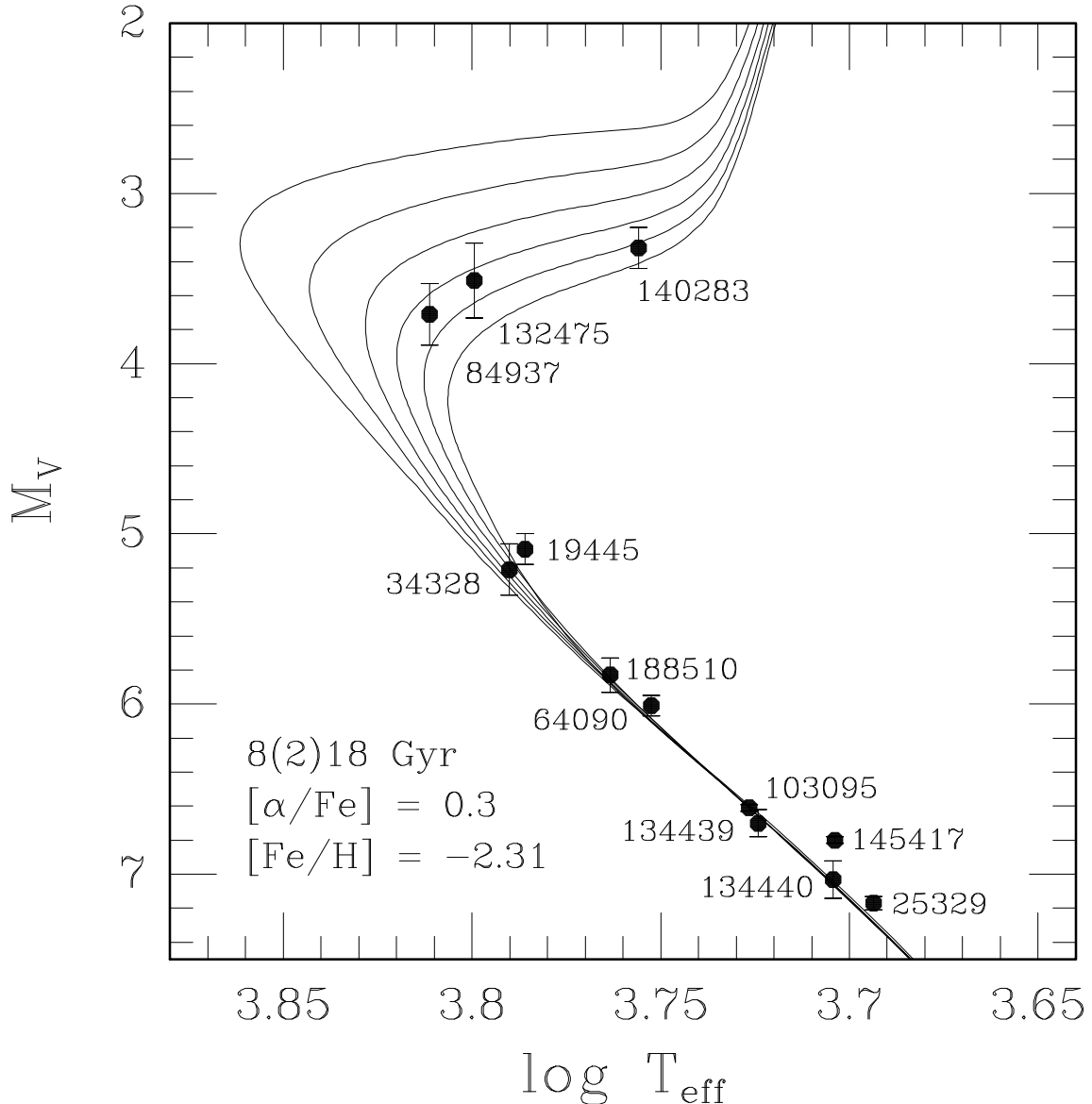


Fig. 6.— Comparison of isochrones for the indicated parameters with the properties of several Population II subdwarfs and subgiants (identified by their HD numbers), after the effective temperatures of the latter were corrected to the values they would have if their iron abundances corresponded to $[Fe/H] = -2.31$. For all but one of the stars, the temperature adjustments that were applied to produce the “mono-metallicity” subdwarf sequence were ≤ 0.017 in $\log T_{\text{eff}}$. Because the point representing HD 132475 involved a rather large temperature adjustment ($\delta \log T_{\text{eff}} = 0.036$), its location in this diagram is arguably the least well determined of all of the stars that have been considered. The sources of the stellar data are given in the text. Note that Lutz-Kelker corrections were applied to the M_V values using the formula adopted by Carretta et al. (2000): these amounted to ≤ 0.04 mag, except in the cases of HD 84937 and HD 132475, for which $\delta M_V^{\text{LK}} = -0.07$ and -0.11 mag, respectively. Neglecting these corrections, which may not be appropriate for this highly-selected sample of stars, would imply slight increases in the ages of the 3 subgiants. Note, as well, that all of the latter appear to be very old stars, with ages near 15–16 Gyr.

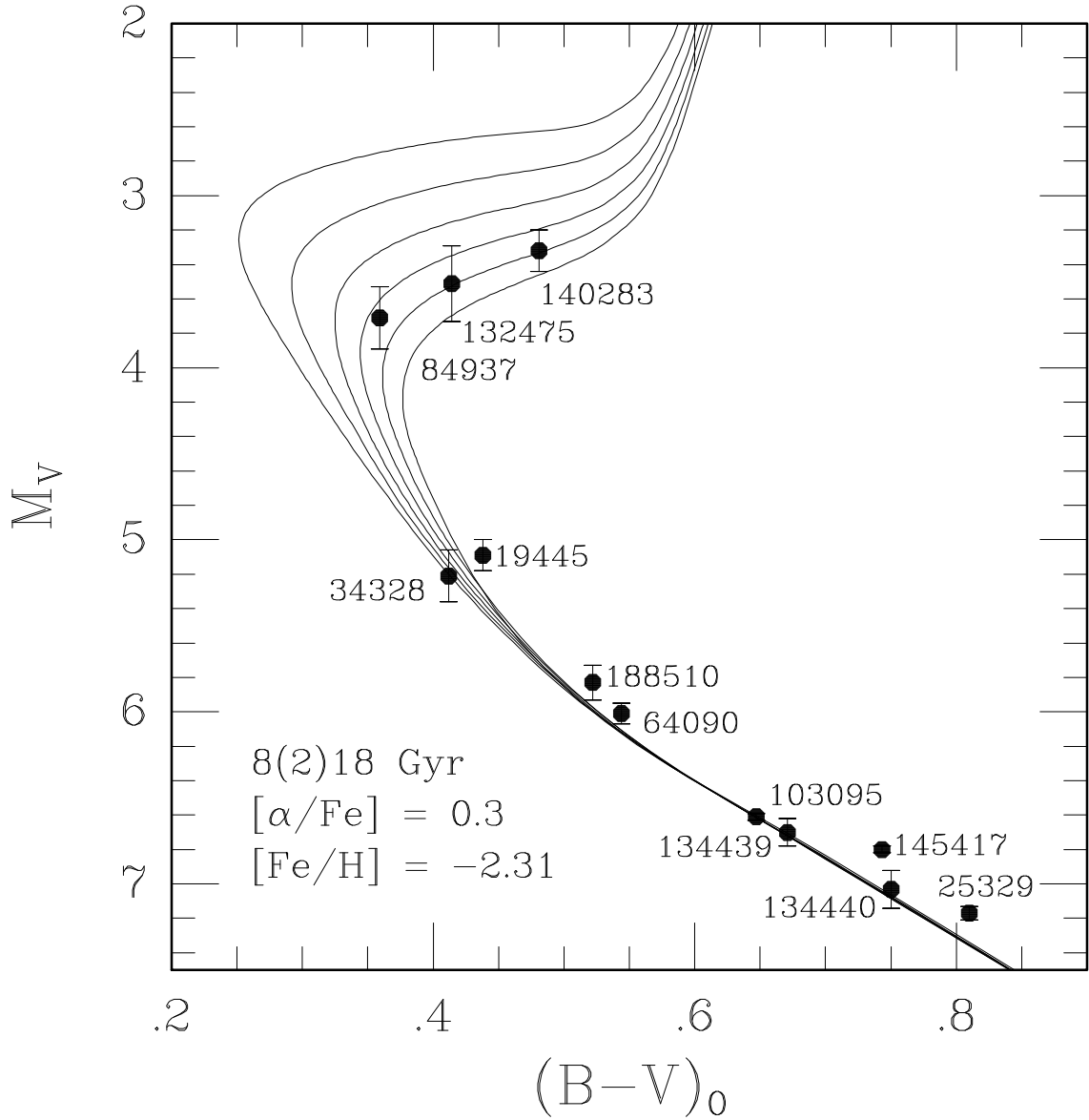


Fig. 7.— Similar to the previous figure, except that comparison is carried out on the $[M_V, (B-V)_0]$ -plane. The observed colors and adopted reddenings of the stars that have been considered are as given by Carretta et al. (2000). In constructing the “mono-metallicity” subdwarf sequence, the corrections that were applied to the intrinsic colors ranged from +0.018 mag (in the case of HD 140283) to -0.108 mag (for HD 132475, whose position in this diagram is especially uncertain).

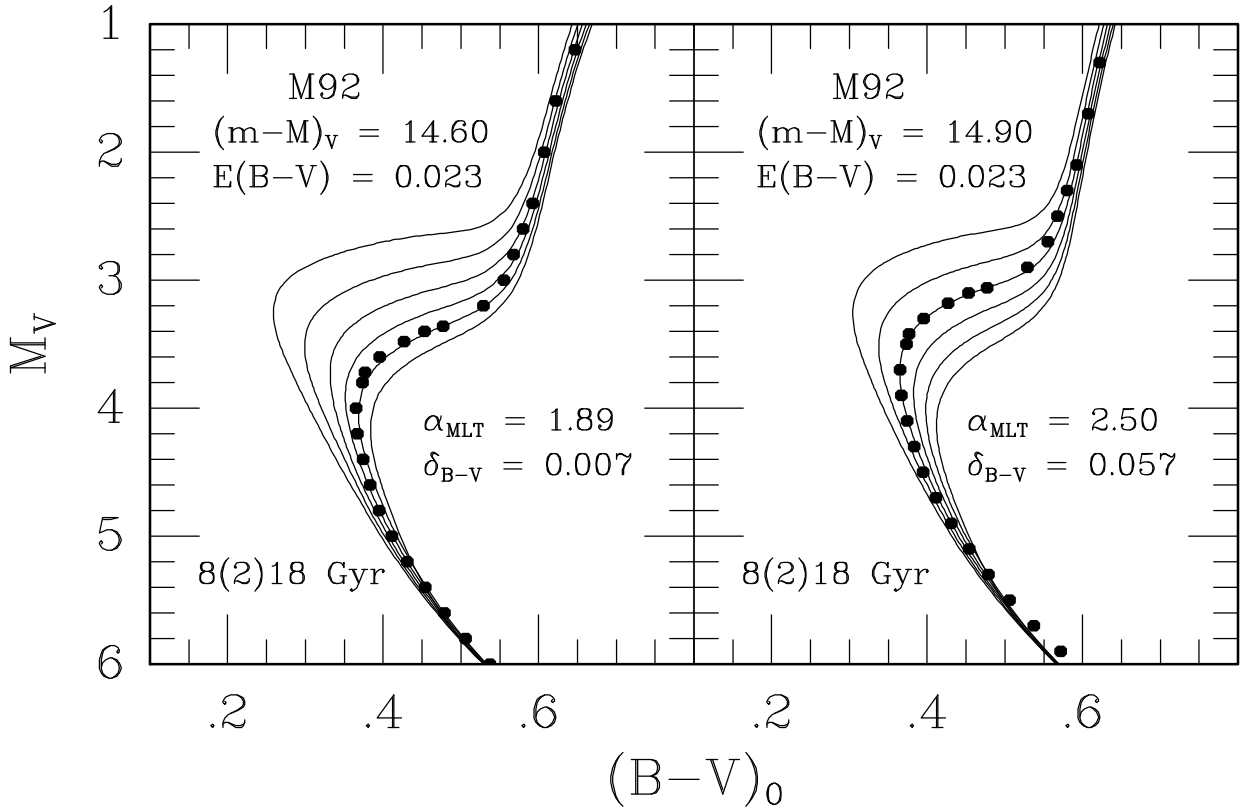


Fig. 8.— Fits of isochrones for $[\text{Fe}/\text{H}] = -2.31$ and $[\alpha/\text{Fe}] = 0.3$ to the Stetson & Harris (1988) fiducial for M 92, supplemented by data for the lower giant branch from M. Bolte (private communication). The Schlegel et al. (1998) reddening estimate has been assumed. The only difference in the models is the value that has been assumed for the usual mixing-length parameter, α_{MLT} . The main point of this figure is that it is possible to obtain comparably good agreement between synthetic and observed C-M diagrams on the assumption of distance moduli that differ by 0.3 mag (and ages that differ by ≈ 4 Gyr) simply by choosing the value of α_{MLT} appropriately. However, very different zero-point offsets must be applied to the colors of the isochrones in order to match the observed turnoffs in the two cases and, on this basis, the comparison given in the left-hand panel is clearly favored over that given in the right-hand panel.

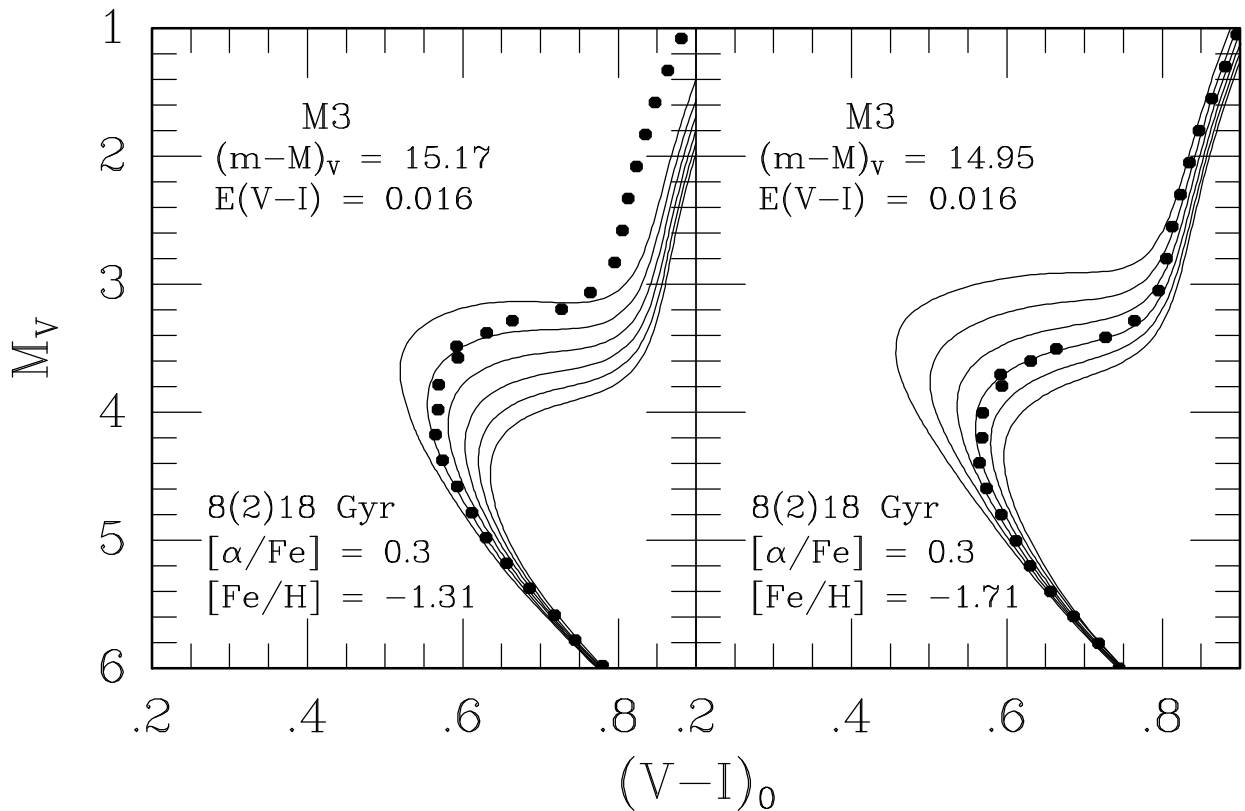


Fig. 9.— Main-sequence fits of the Stetson et al. (1999) fiducial for M3 to isochrones for the indicated parameters. The adopted reddening is consistent with that given by Schlegel et al. (1998).

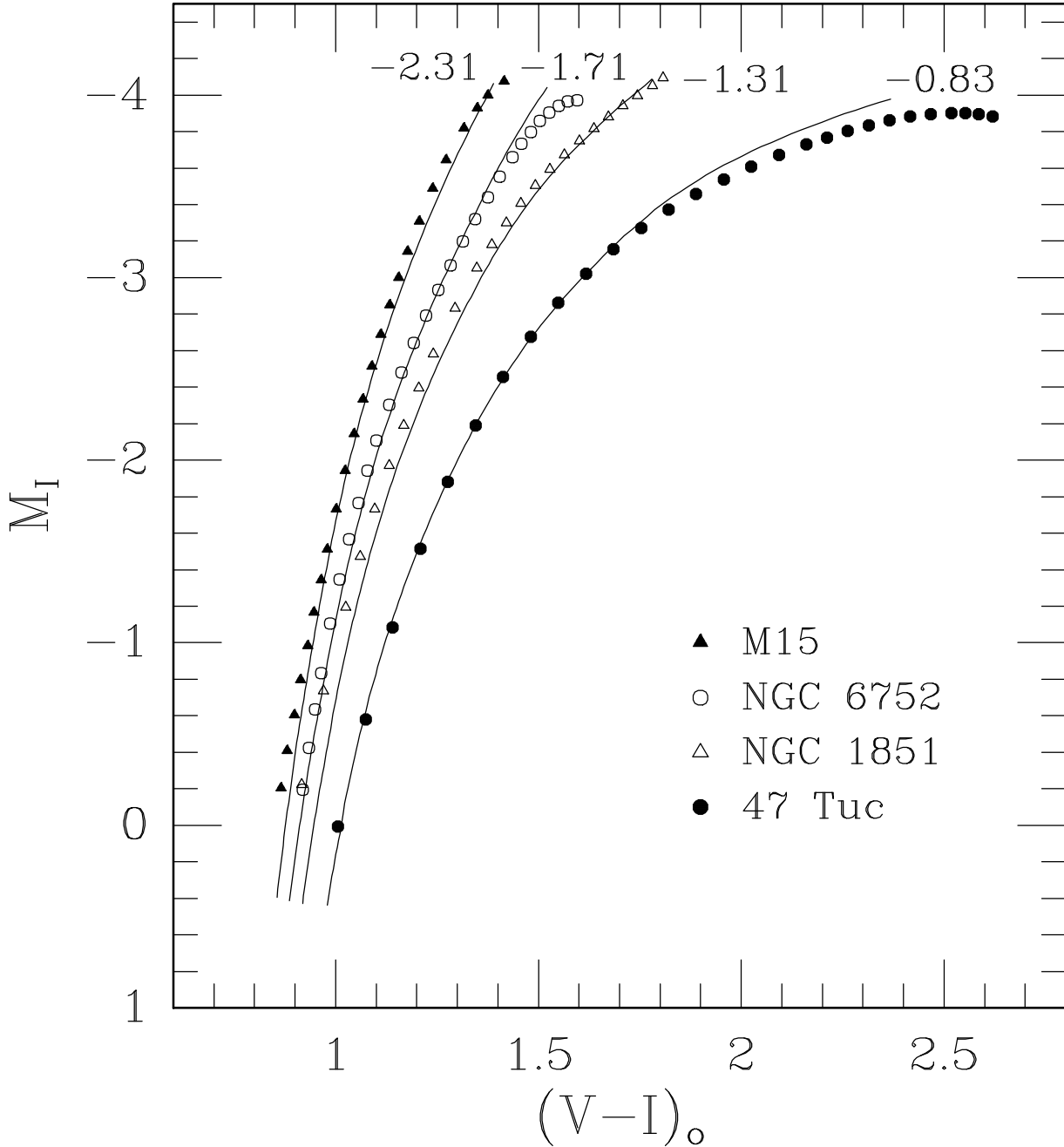


Fig. 10.— Overlay of the giant-branch segments of isochrones for the indicated [Fe/H] values onto the fiducial sequences derived by Da Costa & Armandroff (1990) for M 15, NGC 6752, NGC 1851, and 47 Tuc. For these four clusters, in turn, we have assumed $E(B - V) = 0.108, 0.056, 0.034$, and 0.032 mag (Schlegel et al. 1998), as well as $(m - M)_V = 15.43, 13.25, 15.55$, and 13.37 mag (see Paper II), which imply cluster ages near 14, 13, 11.5, and 11.5 Gyr, respectively (see Paper II). To produce this plot, $A_V = 3.1 E(B - V)$, $A_I = 0.59 A_V$, and $E(V - I) = 1.25 E(B - V)$ have also been assumed (see, e.g., Bessell et al. 1998).

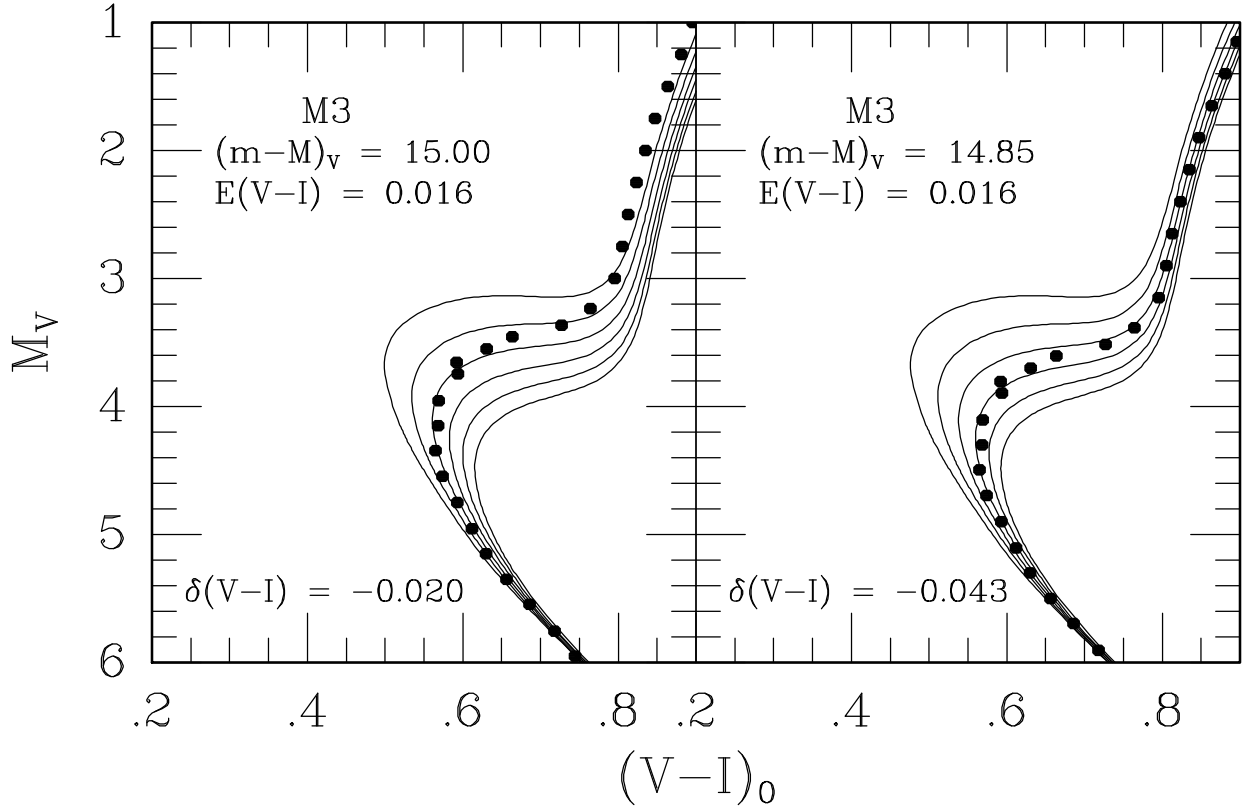


Fig. 11.— Similar to the left-hand panel of Fig. 9, except that the cluster distance modulus has arbitrarily been set to the indicated values. To reconcile the observed turnoff with that of the most appropriate isochrone, the zero-point shift specified in the lower left-hand corner of each panel was applied to the isochrone colors.

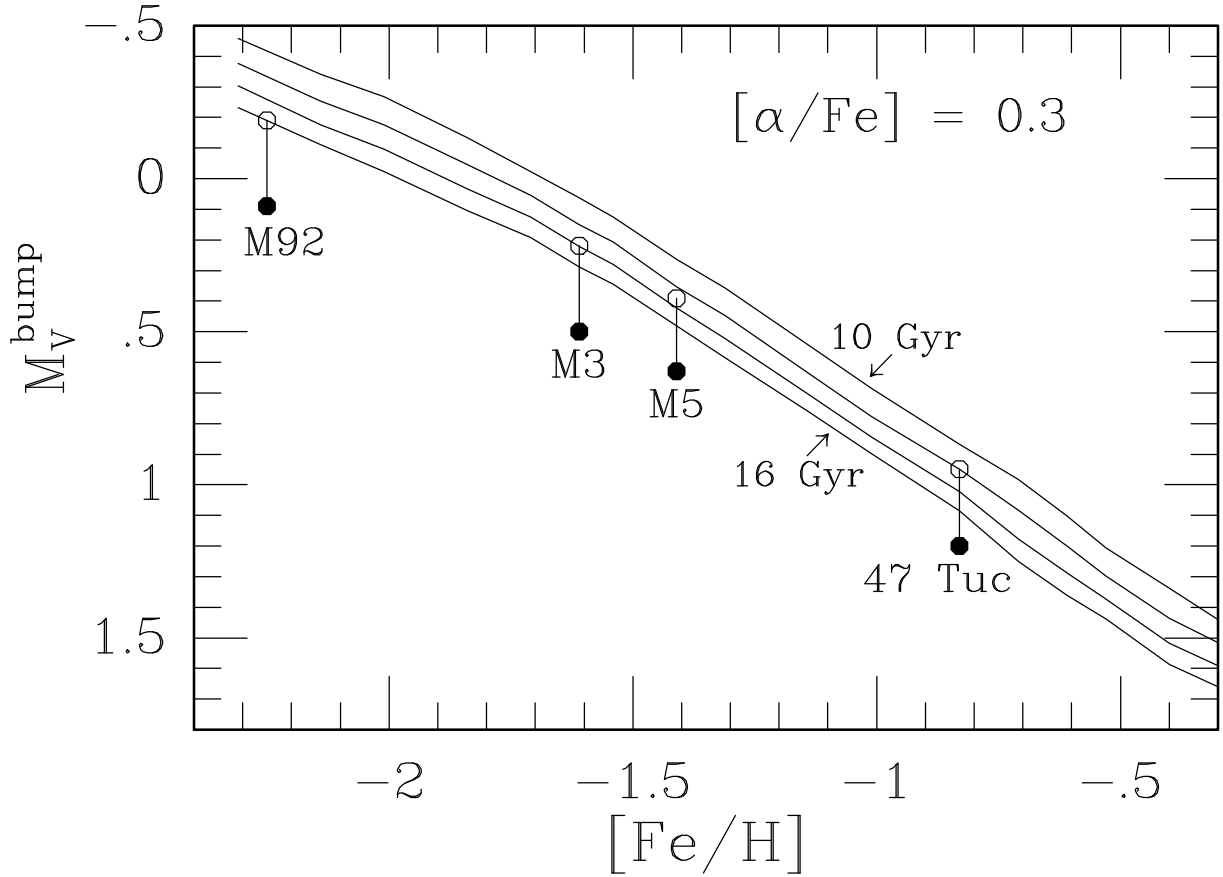


Fig. 12.— Plot of the M_V^{bump} versus $[\text{Fe}/\text{H}]$ data given in Table 6 for $[\alpha/\text{Fe}] = 0.3$ and ages from 10 to 16 Gyr, in 2 Gyr steps. If the ages of M92, M3, M5, and 47 Tuc are 16 Gyr, 14 Gyr, 13 Gyr, and 12 Gyr, respectively (see the text), then the observed magnitudes of the RGB bumps in these clusters are given by the *filled circles*, while the predicted luminosities of this diagnostic are given by the *open circles*.